The 26 December 2001 Solar Eruptive Event Responsible for GLE63. III. CME, Shock Waves, and Energetic Particles

V.V. Grechnev [ORCID] · **V.I. Kiselev**[1] ·
A.M. Uralov[1] · **K.-L. Klein**[2] ·
A.A. Kochanov[1]

© Springer ••••

Abstract The 26 December 2001 moderate solar eruptive event (GOES importance M7.1, microwaves up to 4000 sfu at 9.4 GHz, CME speed $1446\,\mathrm{km\,s^{-1}}$) produced strong fluxes of solar energetic particles (SEPs) and ground-level enhancement of cosmic-ray intensity (GLE63). To find a possible reason for the atypically high proton outcome of this event, we study its multi-wavelength images and dynamic radio spectra, and quantitatively reconcile the findings with each other. An additional eruption probably occurred in the same active region about half an hour before the main eruption, which produced two blast-wave-like shocks during the impulsive phase. Later on, the two shock waves merged around the frontal direction into a single shock, which is traced up to $25\mathrm{R_\odot}$ as a halo ahead of the expanding CME body, in agreement with an interplanetary type II event recorded by *Wind*/WAVES. The shape and kinematics of the halo indicate that the shock wave was in an intermediate regime between the blast wave and bow shock at these distances. The results show that i) the shock wave appeared during the flare rise and could accelerate particles earlier than usually assumed; ii) the particle event could be amplified by the preceding eruption, which stretched closed structures above the developing CME, facilitating its lift-off and escape of flare-accelerated particles, enabling a higher CME speed and a stronger shock ahead; iii) escape of flare-accelerated particles could be additionally facilitated by reconnection of the flux rope, where they were trapped, with a large coronal hole; iv) a rich seed population was provided by the first eruption for the acceleration by a trailing shock wave.

[1] Institute of Solar-Terrestrial Physics SB RAS, Lermontov St. 126A, Irkutsk 664033, Russia; email: grechnev@iszf.irk.ru
email: valentin_kiselev@iszf.irk.ru email: uralov@iszf.irk.ru
email: kochanov@iszf.irk.ru
[2] LESIA-UMR 8109, Observatoire de Paris, CNRS, Univ. Paris 6 & 7, Observatoire de Meudon, F-92195 Meudon, France; email: ludwig.klein@obspm.fr

1. Introduction

Solar energetic particles (SEP), which are somehow accelerated in association with solar eruptive events, offer hazards for equipment and astronauts on spacecraft, and even for crew members and passengers on aircraft in high-latitude flights due to secondary particles produced in the Earth's atmosphere. SEPs mainly consist of protons, alpha particles, and heavier ions. Their energies reach hundreds of MeV and sometimes up to several GeV. The highest-energy extremity of SEPs occasionally produces considerable fluxes of secondary neutrons, which are able to cause ground-level enhancements (GLE) of cosmic-ray intensity. Seventy-two GLEs have been registered since 1942 until the present time mainly with high-latitude neutron monitors (see, *e.g.*, Cliver, 2006; Belov *et al.*, 2010; Nitta *et al.*, 2012; Miroshnichenko, Vashenyuk, and Pérez-Peraza, 2013 and references therein). On average, GLEs occur once a year, but very irregularly. GLEs avoid solar minima, while four GLEs occurred within a week in May 1990. The rare, irregular observations of GLEs hamper understanding their origins and emphasize the importance of studying each solar event responsible for a GLE.

One presumable source of SEPs and GLEs is traditionally associated with flare processes in coronal magnetic fields of active regions exhibited in X-ray and microwave emissions. Another probable source of SEPs is related to bow shocks driven by fast coronal mass ejections (CMEs). In spite of a high practical importance of SEP events, consensus has not been reached so far about the probable contributions from the two sources in different events and energy ranges. The main subject of the debates is related to the origins of high-energy SEPs and especially GLEs (see, *e.g.*, Klein and Trottet, 2001; Kallenrode, 2003; Grechnev *et al.*, 2008a; Reames, 2009a; Aschwanden, 2012; Miroshnichenko, Vashenyuk, and Pérez-Peraza, 2013 for a review and references). Either competing concept is supported by convincing arguments (Tylka *et al.*, 2005; Chupp and Ryan, 2009; Vilmer, MacKinnon, and Hurford, 2011; Rouillard *et al.*, 2012; Reames, 2013).

A traditional view on the SEP origins is mainly based on the hypotheses proposed in the past decades, when observational opportunities were strongly limited relative to the modern ones. Traditional concepts considered the processes responsible for acceleration of particles in flares and those by shock waves to be remote and completely independent of each other. Observational studies of two last decades update the view on solar eruptive phenomena step by step and reveal their close association with each other.

Zhang *et al.* (2001) and Temmer *et al.* (2008, 2010) found synchronization between the CME acceleration pulse and hard X-ray (HXR) and microwave bursts. Qiu *et al.* (2007) established that the helical component of the CME's flux rope (responsible for its acceleration) is formed by reconnection, which caused a flare. Miklenic, Veronig, and Vršnak (2009) found a quantitative correspondence between the reconnected magnetic flux and the rate of flare energy release. Grechnev *et al.* (2011, 2013a, 2015b, 2016) established that waves are impulsively

excited by erupting flux ropes inside developing CMEs during the rise phase of HXR and microwave bursts and rapidly steepen into the shocks due to a rapid falloff of the fast-mode speed. Then the shock wave quasi-freely propagates for some time like a decelerating blast wave and changes to the bow-shock regime later, if the trailing CME is fast.

The listed observational results and outlined scenario show that the traditional contrasting of the acceleration in a flare and by a shock might be exaggerated. Two consequences important for the SEP acceleration problem follow from them. First, shock waves appear much earlier than previously assumed and can accelerate heavy particles even during the flare. Second, a close association is expected between the parameters of the CME, shock wave, and flare, on the one hand, and those of a SEP event.

These circumstances indicate that both flare-related and shock-related acceleration can be significant in SEP production, while their roles might depend on particular conditions in different events. Recent studies by Dierckxsens *et al.* (2015); Trottet *et al.* (2015); Grechnev *et al.* (2015a) confirmed this idea and indicated statistically increasing importance of the flare-related particle acceleration at higher energies. The shock-related contribution was also manifest.

In Article I (Grechnev and Kochanov, 2016) and Article II (Grechnev *et al.*, 2017) we started analyzing the 26 December 2001 event related to an M7.1 flare with a peak time at 05:40 (all times hereafter refer to UTC if not specified otherwise) responsible for GLE63. Among all GLE-related flares of Solar Cycle 23, this flare had a lowest GOES importance and longest duration, being associated with a microwave burst of a relatively moderate intensity. Limited observations of the flare and eruption determined incomplete knowledge of this solar event. No soft X-ray (SXR) images or HXR data are available. Observations with the *Extreme-ultraviolet Imaging Telescope* (EIT: Delaboudinière *et al.*, 1995), onboard the *Solar and Heliospheric Observatory* (SOHO), had a gap from 04:47 to 05:22.

Some aspects of this event look challenging. If protons and heavier ions were accelerated in the flare concurrently with electrons, then it is not clear why their fluxes were so large. If they were shock-accelerated, then it is not clear why the fast CME and strong shock developed in association with a moderate flare. It is also not clear when and where the shock wave appeared and how it evolved.

Articles I and II analyzed the event from microwave imaging observations with the *Siberian Solar Radio Telescope* (SSRT: Smolkov *et al.*, 1986; Grechnev *et al.*, 2003) at 5.7 GHz; the *Nobeyama Radioheliograph* (NoRH; Nakajima *et al.*, 1994) at 17 and 34 GHz and total flux data of *Nobeyama Radio Polarimeters* (NoRP: Nakajima *et al.*, 1985), and the ultraviolet (UV) images from the *Transition Region and Coronal Explorer* (TRACE: Handy *et al.*, 1999) in 1600 Å.

The results of Articles I and II related to the particle event are as follows.

1. GLE63 was most likely caused by the M7.1 event in active region (AR) 9742 (N08 W54). Implication of a hypothetical concurrent far-side event is unlikely.
2. The flare was much longer than other GLE-related flares and consisted of two parts, each of which was most likely caused by a separate eruption.
3. The first eruption presumably occurred in AR 9742 around 04:40 and produced an ejecta, which was not observed. A related moderate two-ribbon flare involved medium magnetic fields and reached a GOES importance of M1.6.

4. The second eruption occurred in AR 9742 around 05:04 and produced a fast CME. The related main two-ribbon flare involved strong magnetic fields associated with a sunspot and reached an importance of M7.1.
5. An extra sharp jet-like eruption around 05:09 could produce a shock wave.

Based on these results, in this article we analyze the eruptions in this event from indirect observations. We endeavor to reconstruct the CME and shock wave, their evolution, and to find which circumstances could amplify the SEP outcome of this event. Pursing the last issue, we compare the 26 December 2001 event with other SEP and GLE events. Invoking the recent observational conclusions about scenarios of the CME and shock-wave development listed in this section, we revisit this historical GLE-related event on the basis of the modern view.

Section 2 presents the main features of the SEP event. Section 3 outlines the flare and reveals the eruptions. Section 4 analyzes drifting radio bursts observed in a wide frequency range to reconstruct the history of the eruptive event and reveal the shock wave. A long-standing issue of the relation between metric and interplanetary Type II events is also addressed. Section 5 considers the CME. Section 6 discusses the results, evolution of the CME and shock wave, indications of particle release, and the possible causes of the enhanced SEP outcome of this event. Section 7 summarizes the conclusions of the study.

2. Particle Event

In this section we overview the SEP event on 26 December 2001, which is of a special interest. To get hints at the possible causes of an enhanced SEP outcome of its solar source, we compare selected properties of the SEP event with some other SEP and GLE events.

2.1. Near-Earth Proton Enhancement

SEPs are dominated by accelerated protons. Figure 1 presents two-day time-profiles of the SXR flux from the flare and the proton flux in three standard integral channels of GOES-8. Figure 1b additionally shows the flux of high-energy protons > 700 MeV recorded by the *High-Energy Proton and Alpha Detector* (HEPAD) on GOES-8 magnified by a factor of 100.

The time-profiles of the proton fluxes are typical for well-connected events, with a sharp rise approximately corresponding to the flare peak followed by a moderately long decay. HEPAD detected a highest-energy > 700 MeV enhancement, which appears to be typical of GLE events. The pre-event background does not show any elevated seed population, as was the case before GLE33 and GLE35 addressed by Cliver (2006), and his conclusion about these events does not provide a straightforward key to understanding GLE63.

Mewaldt *et al.* (2012) presented the energy spectra of proton fluences and other SEP properties during the 16 GLEs of Solar Cycle 23. The spectra in a range of $\sim 0.1 - 600$ MeV are best fit with double power-laws. On average, the spectra above ~ 40 MeV in GLE events have a slope of -3.18 with $\sigma = 0.83$, significantly harder than in typical large SEP events (-4.34, $\sigma = 0.77$).
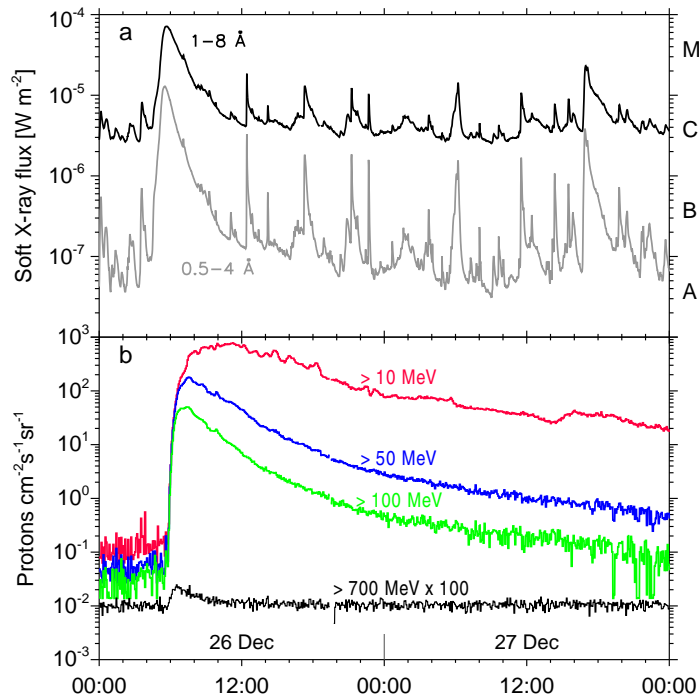
Figure 1. Time profiles of the soft X-ray flux (a) and near-Earth proton enhancement (b) recorded by three standard integral channels of GOES-8 and the high-energy HEPAD detector ($> 700\,\mathrm{MeV}$: black, magnified by a factor of 100).

The spectral slopes below the break-energies are similar, being about -1.25 on average. The spectrum of the proton fluence in our event had a slope of -1.53 below $32\,\mathrm{MeV}$ and -3.14 at higher energies, close to the average values for other GLEs. Different authors discuss the appearance of the double power-law spectral shape. On the other hand, domination of shock-acceleration at lower energies and flare-acceleration at higher energies (Miroshnichenko, Vashenyuk, and Pérez-Peraza, 2013) seems to be also possible, especially in the spectra of the proton fluences integrated over the whole SEP event lasting a few days.

2.2. Some Properties of Heavier Ions

The SEP events have traditionally been categorized as gradual or impulsive events (mixed events are also considered). Gradual SEP events are characterized as long-duration, large, intense events. They have average ion abundances similar to those of the corona or solar wind. In contrast, impulsive SEP events are small, have relatively short durations, can have 1000-fold enhancements in $^3\mathrm{He}/^4\mathrm{He}$ and in heavy elements $(Z > 50)/\mathrm{O}$ relative to the corona or solar wind, and are associated with solar flares or jets and type III radio bursts (Reames, 2013). The 26 December 2001 event had a long duration and low $^3\mathrm{He}/^4\mathrm{He}$ ratio like gradual events (Desai *et al.*, 2006), but also had some properties of impulsive events.

Mewaldt *et al.* (2012) discussed such property of the SEP composition as the Fe/O ratio, which is often considered as diagnostics of flare material. The Fe/O ratio typical of impulsive flare-related SEPs is about unity, while that of gradual shock-accelerated SEPs is, on average, around 0.1, with a criterion for Fe-rich GLE events of Fe/O $\geq$ 0.268 (Tylka *et al.*, 2005). The authors of both studies noted that the Fe-rich GLEs, on average, have much smaller $> 30\,\mathrm{MeV}$ proton fluences than the Fe-poor GLEs. In our event, the Fe/O ratio in the range 45 to 80 MeV/nucleon was 0.671, and the $> 30\,\mathrm{MeV}$ proton fluence was $1.16 \times 10^7\,\mathrm{protons\,cm^{-2}}$, while this parameter for the 16 GLEs was in the range $(8.02 \times 10^6 - 4.31 \times 10^9)\,\mathrm{protons\,cm^{-2}}$ with a logarithmic average of $1.77 \times 10^8\,\mathrm{protons\,cm^{-2}}$. Tylka *et al.* (2013) argued the initial Fe/O enhancement in the 26 December 2001 SEP event to be a transport effect. If so, then the pattern established by Tylka *et al.* (2005) and Mewaldt *et al.* (2012) between the Fe/O ratio and the $> 30\,\mathrm{MeV}$ proton fluence did not hold in this event.

A promising characteristic of the equilibrium temperature in the acceleration region is the mean ionic charge state of iron, $\langle Q_{\mathrm{Fe}} \rangle$. In 10 out of the 16 GLEs, in which it was measured, $\langle Q_{\mathrm{Fe}} \rangle$ ranged from 11.7 to 22.1. In our event, $\langle Q_{\mathrm{Fe}} \rangle = 20.7$ corresponds to about $10\,\mathrm{MK}$, which seems to indicate flare material. Mewaldt *et al.* (2012) point out that the highly-ionized $> 20\,\mathrm{MeV/nucleon}$ ions in this event and some others could also be the result of electron stripping during the acceleration and/or transport process in a sufficiently dense ambient plasma. The authors concerned with this effect consider that, in terms of the traditional concept (*e.g.* Reames, 2009a, 2013), a CME-driven bow-shock appears and can start accelerating ions between ~ 140 and $\sim 400\,\mathrm{Mm}$ above the photosphere. On the other hand, recent results listed in Section 1 show that the shock-acceleration can occur in still lower corona, and it is surprising why electron stripping is not common, so that high $\langle Q_{\mathrm{Fe}} \rangle \approx 20$ are not always observed.

Thus, the studies of low to moderate energy protons and heavier ions reveal indications of both shock-related and flare-related contributions in the 26 December 2001 event. However, the latter are not certain and can be interpreted in different ways. Note that the results of these studies were interpreted in terms of old hypotheses, while their update might lead to different conclusions.

2.3. Highest-Energy Particles

The highest-energy manifestations of SEPs on 26 December 2001 are shown in Figure 2. A proxy of ground-level events is presented by the HEPAD proton channel $> 700\,\mathrm{MeV}$ in Figure 2a. It does not always show a one-to-one correspondence with GLEs, for which particles (mainly protons) of still higher energies, $\gtrsim 1\,\mathrm{GeV}$, are responsible (Miroshnichenko, Vashenyuk, and Pérez-Peraza, 2013). Figure 2b shows GLE63 as recorded by the Apatity and Oulu neutron monitors. The vertical dashed line denotes the solar particle release time (SPR), 05:20.6 ST $\pm 3.7\,\mathrm{min}$ (Solar Time refers to an event on the Sun, leading UTC by the propagation time of light, *i.e.* 05:29:00 UTC $\pm 3.7\,\mathrm{min}$), estimated by Reames (2009b) from the velocity dispersion analysis (VDA).

A possible indication of heavy ions accelerated to still higher energies in our event is presented by preliminary data from the *Trans-Iron Galactic Element*
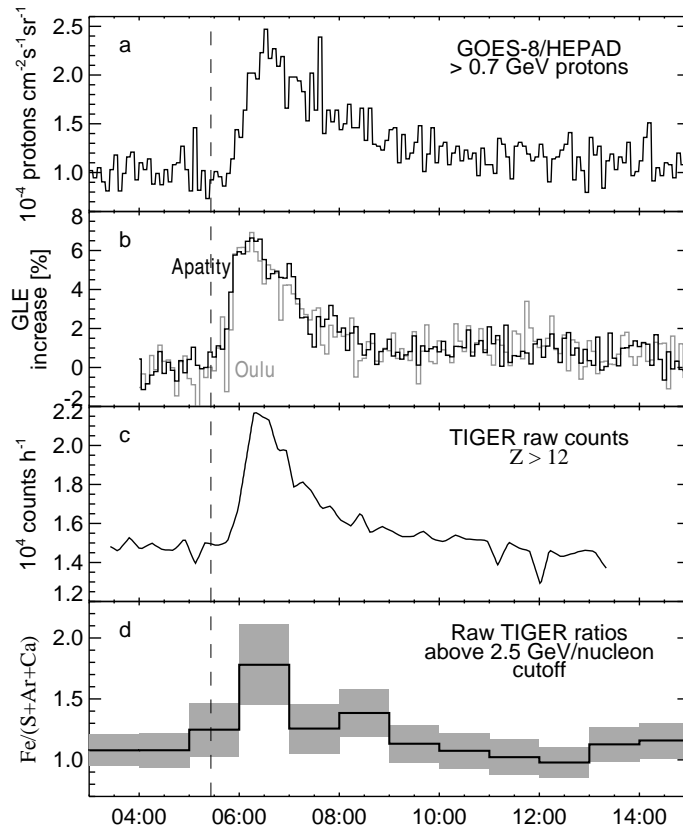
Figure 2. Data on high-energy heavy particles. a) GOES-8/HEPAD P11 proton channel > 700 MeV. b) GLE recorded with the Apatity (black) and Oulu (gray) neutron monitors. c) Raw record of the Antarctic TIGER balloon experiment of response to high-energy ions with $Z \geq 13$. d) Raw ratios of heavy ions above the 2.5 GeV/nucleon cutoff calculated from the TIGER data. The vertical dashed line denotes the particle release time (Reames, 2009b).

Recorder (TIGER: Geier *et al.*, 2003). TIGER was launched on 21 December 2001 and flew for about 32 days on a long-duration balloon mission from Mc-Murdo Base in Antarctica. Being designed mainly to measure the elemental abundances of galactic cosmic ray nuclei, TIGER likely observed the 26 December 2001 GLE event in the $\sim$ GeV/nucleon range. Figure 2c shows raw counts produced by heavy elements with $Z > 12$ traversing raw triggers of the device. The shape of the raw TIGER flux is very similar to that measured by neutron monitors in Figure 2b, manifesting the common origin of detected events. No similar deviations from the data gathered during the other time intervals of the flight were observed. Figure 2d shows the ratios of heavy elements that reached the C0 TIGER Cherenkov detector. An interesting point here is that the estimated lower-energy limit of particles that can trigger the C0 detector is around 2.5 GeV/nucleon. During the event, the efficiency of the TIGER track-reconstruction software dropped from $\approx 80\%$ to under $\approx 60\%$, resulting in an additional dead time, that might affect the measured ratio (Geier *et al.*, 2003).

Still Figure 2d shows more iron and presents unique evidence that heavy ions could be accelerated to such high energies during this event.

Acceleration of protons and heavier ions in the 26 December 2001 event up to relativistic energies is certain. However, we have not found so far clear indications of the SEP sources. One more indication can possibly be found from statistical relations between parameters of SEPs, on the one hand, and those of flares and CMEs, on the other hand.

2.4. Protons *vs.* 35 GHz Bursts and CMEs Statistics

The correlation between near-Earth proton enhancements and microwave bursts has been known for a long time (Croom, 1971; Castelli and Barron, 1977; Akinian *et al.*, 1978; Melnikov *et al.*, 1991). Kahler (1982) explained this correlation by the 'big flare syndrome' (BFS), *i.e.*, a general correspondence between the energy release in an eruptive flare and its various manifestations. According to his idea, SEPs are accelerated by shock waves, while different parameters of eruptive events should correlate with each other, independent of any physical connection between them. Supporting this concept, Kahler (1982) analyzed the correlations between the peak proton fluxes at $20-40\,\mathrm{MeV}$ and $40-80\,\mathrm{MeV}$ in 50 SEP events observed in $1973-1979$, on the one hand, and microwave data at $8.8\,\mathrm{GHz}$, $15.4\,\mathrm{GHz}$, and two lower frequencies, on the other hand, using the lists of selected parameters. No proxy of any shock parameters was available. Kahler (1982) found that the peak proton fluxes correlated with microwaves not higher than with the thermal SXR flare emission. Having assumed that protons accelerated either by flares or by shocks and not by both, he favored the shock-acceleration. This conclusion resulted in a prevalent sceptical relation to the correlations between the parameters of SEPs and microwave bursts.

Rethinking the role of the BFS is inspired by recent studies of Grechnev *et al.* (2013b, 2015a). They analyzed the relations between the parameters of strong microwave bursts $> 1000\,\mathrm{sfu}$ at $35\,\mathrm{GHz}$ using a homogeneous series of NoRP observations in $1991-2012$, on the one hand, and near-Earth proton enhancements $> 100\,\mathrm{MeV}$, on the other hand, using detailed time histories. The use of the high observing frequency reduces the ambiguity of its possible position relative to the burst's peak frequency. Proton enhancements $> 100\,\mathrm{MeV}$ with peak fluxes $J_{100} > 10\,\mathrm{pfu}$ ($1\,\mathrm{pfu} = 1\,\mathrm{particle\,cm^{-2}\,s^{-1}\,sr^{-1}}$) were also considered not to miss big SEPs after weaker bursts occurring during the observations of NoRP.

Out of the total set of events, 28 SPEs in $1996-2012$ were selected, whose sources were not occulted and data on the corresponding CMEs are listed in the online CME catalog (cdaw.gsfc.nasa.gov/CME_list/: Yashiro *et al.*, 2004) based on the observations by the SOHO's *Large Angle and Spectroscopic Coronagraph* (LASCO: Brueckner *et al.*, 1995). Because the speeds listed in the CME catalog are measured for a fastest feature, V_{CME} for fast CMEs are most likely related to shock waves (Ciaravella, Raymond, and Kahler, 2006). The halo shock fronts ahead of fast CMEs should have the shapes close to spheroidal ones (Grechnev *et al.*, 2011, 2013a, 2014b; Kwon, Zhang, and Olmedo, 2014; Kwon, Zhang, and Vourlidas, 2015); thus, the plane-of-the sky speeds measured in the catalog
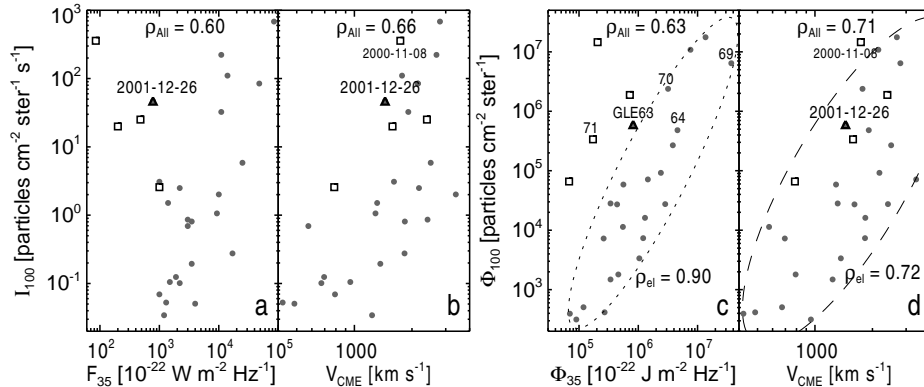
Figure 3. Near-Earth high-energy proton enhancements and strong microwave bursts recorded by NoRP at 35 GHz in 1996 – 2012 (partly adapted from Grechnev *et al.*, 2015a). Scatter (log–log) plots present the longitude-corrected parameters of $> 100\,\mathrm{MeV}$ protons (peak flux I_{100} in the left pair of panels, total fluence Φ_{100} in the right pair of panels) versus parameters of microwave bursts at 35 GHz (peak flux F_{35} left, fluence Φ_{35} right) and CME speed. The broken ellipses in panels c and d enclose the majority of the events. The Pearson correlation coefficients at the tops of the panels were calculated for all 28 events (ρ_{All}), and those at the bottoms of panels c and d (ρ_{el}) are related to the events within the ellipses. The open squares denote the events with abundant proton outcome. The filled triangle denotes the 2001-12-26 event. The GLE numbers are indicated at corresponding points in panel c.

should not be much different from the modules of their vectors ('space speeds'), especially in the logarithmic scale.

Figure 3 (adapted from Grechnev *et al.*, 2015a) presents the results of this analysis. Figure 3a shows the scatter plot of the peak proton flux, J_{100}, *versus* peak microwave flux, F_{35}. The open squares and black triangle (our event) represent the SEPs with $J_{100} > 10\,\mathrm{pfu}$ related to the bursts with $F_{35} \leq 1000\,\mathrm{sfu}$. These five points are considerably displaced away from the majority of SEPs denoted by the gray filled circles, which show a scattered tendency connecting F_{35} and J_{100}. This figure is analogous to what Kahler (1982) presented for lower proton energies and shows a similar result. The Pearson correlation coefficient between V_{CME} and J_{100} in Figure 3b is higher by 10%, and the five proton-abundant events fall mostly within the main cloud of points.

The situation becomes clearer, if total proton fluences Φ_{100} are compared with total microwave fluences Φ_{35} and with V_{CME} in Figures 3c and 3d. While the correlation coefficients increase relative to the left panels by $(5 - 8)\%$ only, two groups of events show up in Figure 3c. The first-group events (gray circles; $F_{35} \geq 10^3\,\mathrm{sfu}$) form a rather narrow cloud within the dotted ellipse with a correlation coefficient as high as 0.90. The five proton-abundant events of the second group (with $F_{35} \leq 10^3\,\mathrm{sfu}$) remain isolated, although approach the main cloud of points. The points in Figure 3d are distributed within the dashed ellipse rather uniformly; the only outlier is the big $8 - 9$ November 2000 event (*e.g.* Lario, Aran, and Decker, 2009) located not far from the ellipse (the correlation coefficients rather than the scale-dependent eccentricities of the ellipses are significant).

An apparent interpretation of Figure 3c is that the first-group well-correlated SEPs were dominated by the flare-related acceleration, because the total number

of protons should depend on both the intensity of the acceleration process and its duration. The correspondence between these parameters of the acceleration process and microwave burst is obvious, but not expected, if protons are accelerated by shock waves far away from a flare region. On the other hand, the shock-related acceleration seems to have dominated in the second-group events. This idea is supported by the relatively uniform distribution of the events within the dashed ellipse in Figure 3d. Nevertheless, the closer location of the proton-abundant events to the main cloud of points in Figure 3c relative to Figure 3a supports the flare-related contribution in these events, too. Without the 8 December 2000 event, the correlation coefficient between Φ_{35} and Φ_{100} in Figure 3c is $\rho_{\mathrm{All}} = 0.74$, higher than between V_{CME} and Φ_{100} in Figure 3d without this event, $\rho_{\mathrm{el}} = 0.72$.

The asymmetry of flare magnetic configurations causes an additional scatter in the correlations between microwave bursts and SEPs. This asymmetry in the 26 December 2001 event reduced the microwave burst by a factor of two with the same production of accelerated particles (Article II).

GLE64, GLE69, and GLE70 fall within the dotted ellipse, belonging to the first group. GLE71 looks like a shock-dominated event. GLE63 seems to have important contributions from both flare-related and shock-related accelerations.

The high correlation for the first-group events within the ellipse in Figure 3c holds over three orders of magnitude for the microwave fluence and five orders for the proton fluence, while V_{CME} in Figure 3d range within one order of magnitude. The general pattern emphasized by Kahler (1982) in terms of the BFS appears to be more complex than correlation between everything in big flares. A general correspondence between parameters of flares, CMEs, shock waves, and SEPs holds in a wide range of their magnitudes. According to Dierckxsens *et al.* (2015) and Trottet *et al.* (2015), the shock-related contribution statistically dominates at lower SEP energies with a major role of flares at higher energies, where shock-accelerated particles also show up (Cliver, 2006; Gopalswamy *et al.*, 2015).

Based on these facts and considerations, it is reasonable to expect that particle acceleration by both flare processes and shock waves contributed to the SEP event on 26 December 2001. We use this assumption as a guideline in our analysis.

3. Eruptions

The eruptive flare on 26 December occurred in AR 9742 not far from the west limb (N08 W54). Figure 4 presents an EIT 284 Å image observed on 20 December, 130 hours before the event. The cross denotes the position of the flare in AR 9742, and the asterisk represents its actual position on 26 December. AR had a $\beta\gamma$ magnetic configuration. Approximate positions of the ends of the erupted flux rope and their magnetic polarities revealed by the flare ribbons and magnetogram are denoted S and N. A large S-polarity coronal hole opposite to AR resided in the southern hemisphere.

Figure 5 presents the active region observed on 26 December by TRACE in 1600 Å (see Article II for more details). The whole event consisted of the first flare (Figure 5a) and the main flare (Figure 5b).
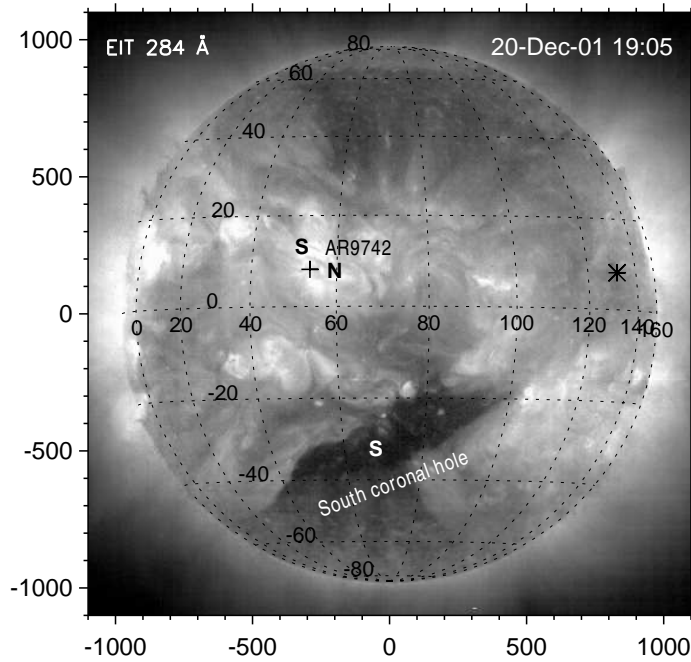
Figure 4. The overall situation on the Sun observed by SOHO/EIT in 284 Å on 20 December. The reported position of the 26 December flare in AR 9742 is denoted by the cross. A large coronal hole is present in the south hemisphere. Magnetic polarities S and N in the coronal hole and in AR 9742 are indicated. The heliographic grid corresponds to the flare occurrence time. The asterisk denotes the actual position of the 26 December flare on the solar disk. The axes indicate the distance from solar disk center in arcseconds.

3.1. First Eruption

The first flare, which was most likely eruptive, started from the appearance of two long, thin, strongly sheared ribbons (Figure 5a). The west ribbon was close to the sunspot. The east ribbon was located in moderate magnetic fields. The SXR flux in Figure 6a started to rise after 04:30 and reached a GOES importance of about M1.6 to 05:04. A dark-gray bar in Figure 6a represents the time interval, in which a slowly-drifting type II and/or type IV burst was observed. Figure 6b shows the time-profiles computed from the TRACE 1600 Å images over the major regions outlined in Figure 5 with corresponding colors. Both ribbons show a rather gradual rise by 05:04.

A slowly-drifting type II and/or type IV burst in an interval marked in Figure 6a could only be caused by an expanding ejecta or wave from AR 9742, which started, at least, ten minutes before the main fast CME. This burst indicates a moderate eruption preceding the fast CME.

Manifestations of the first eruption in running-difference EIT 195 Å images are presented in Figure 7. The top of faint off-limb loop-like features E1 in the pre-eruption (Figure 7a) is outlined by the black arc. This top is displaced slightly in the initiation phase at 04:34:52 in Figure 7b and strongly in Figure 7c at 04:46:52, when it acquired considerable speed and became bright. The lift-off
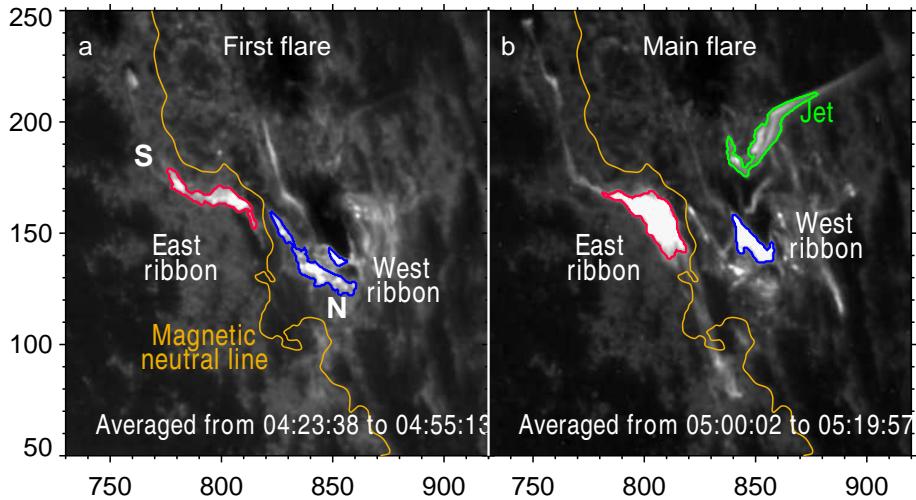
Figure 5. Two parts of the two-ribbon flare represented by TRACE 1600 Å images averaged during the first flare (a) and main flare (b). The blue contours outline the west flare ribbons in the sunspot. The red contour outline the east ribbon in a weaker-field region. The orange contour traces the magnetic neutral line. Magnetic polarities S and N are indicated. The green contour in panel b outlines the brightest portion of the jet and a part of its base. The axes indicate the distance from solar disk center in arcseconds.

of these loops apparently stretched closed coronal structures above them. A dark dimming-like region above the limb started developing behind E1. The images in Figure 7 provide the projected heights of E1 at three times.

3.2. Main Eruption

The main flare, whose start at 05:04 is close to the CME onset time estimated in the CME catalog (light-gray bar in Figure 6a; see also Article II), is characterized by strongly increased emissions from both ribbons in 1600 Å and in microwaves. The west ribbon approached the sunspot umbra and partly covered it. The east ribbon lengthened and broadened, developing into weaker-field regions. The SXR flux strengthened and eventually reached an M7.1 importance at 05:40.

The EIT 195 Å difference image in Figure 8 presents the traces of the associated main eruption, which occurred between 04:47 and 05:22, consistent with an assumed time of 05:04. Coronal structures are strongly disturbed. A large dimming surrounded by stretched loops appears above the limb. The flare configuration is indecipherable in the EIT image because of a low brightness threshold we applied to detect faint features. The flare region with a two-ribbon structure and a bright jet is presented by a higher-resolution TRACE 1600 Å image in the inset, whose actual position is denoted by the white frame.

3.3. Jet

A jet (green in Figures 5 and 6b) appeared after 05:06 from a funnel-like structure, while brightenings ran along its circular base. The time-profile of the jet in
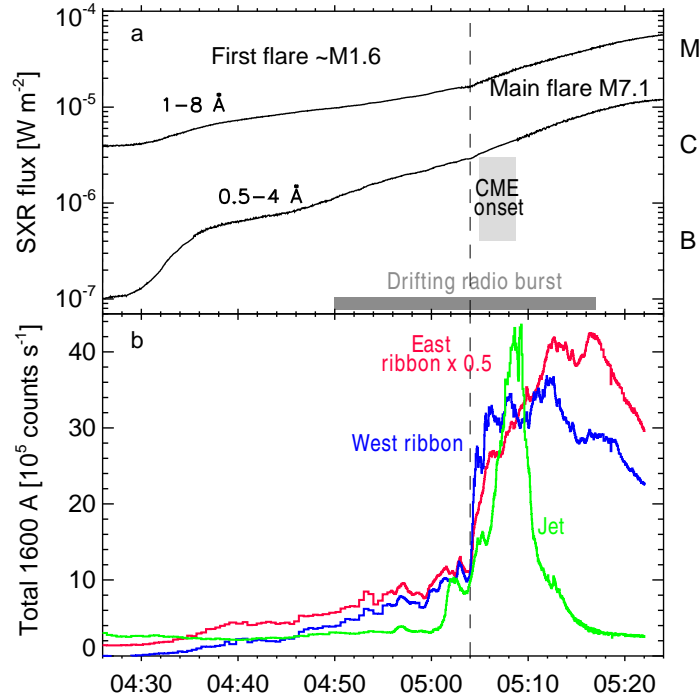
Figure 6. Flare light curves recorded by GOES in soft X-rays (a) and those computed from TRACE 1600 Å images in Figure 5 over the flaring regions presented with the corresponding colors (b). Two flare parts are separated by the vertical dashed line. The gray bars in panel a represent the observation interval of a slowly drifting radio burst and the CME onset time extrapolated to the position of AR 9742.
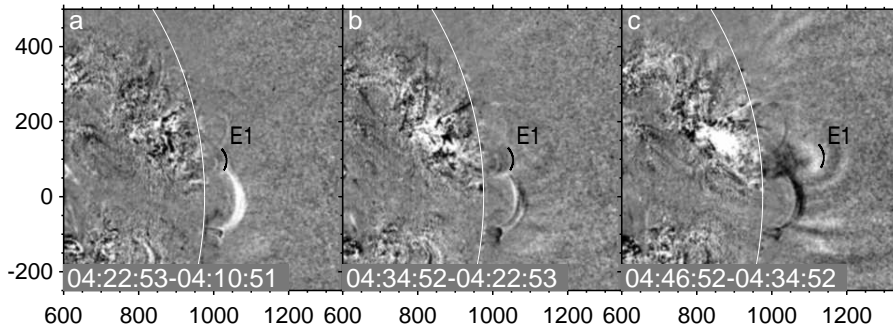
Figure 7. First eruption in running-difference EIT 195 Å images. a, b) Slow expansion of coronal structures in the initiation phase. The black arc denoted E1 outlines the visible top of the rising structures. c) Manifestations of the eruption in the stretched coronal structures. The axes indicate the distance from solar disk center in arcseconds.
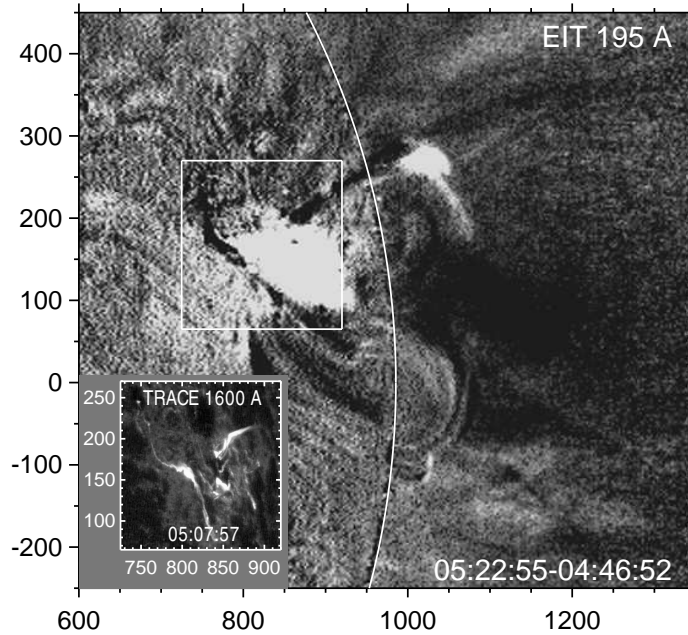
Figure 8. Traces of the main eruption in the EIT 195 Å difference image. The inset presents a TRACE 1600 Å image near the flare peak. Its actual position is denoted by the white frame. The axes indicate the distance from solar disk center in arcseconds.

1600 Å reached a peak at about 05:09, being as short as three minutes at half-height. Figure 9 presents the jet-like eruption. A combined image in Figure 9a composed from an EIT 195 Å image and an averaged TRACE 1600 Å image reveals a large-scale configuration, in which the jet occurred. Figure 9b reveals the structure of the small configuration, from which the jet emanated. This is an enlarged variance image of the jet computed from the TRACE 1600 Å images in an interval from 05:08 to 05:15. This image represents all changes occurring in this interval according to their statistical contributions (Grechnev, 2003).

The coronal configuration in Figure 9b resembles an inverted funnel. Such funnels appear above photospheric magnetic islands inside opposite-polarity regions and contain coronal null points (Masson *et al.*, 2009; Meshalkina *et al.*, 2009). The presence of a magnetic island at the photospheric base of the jet was revealed in Article II. A long tube-like extension (dark in the EIT image in Figure 9a) connects the ring base of the funnel with a remote magnetically conjugate region far away from AR 9742. Magnetic structure of a small flux rope erupting inside a funnel cannot survive when passing at a null point (Uralov *et al.*, 2014) and released plasma flows out as a jet (Filippov, Golub, and Koutchmy, 2009). Jet-like eruptions in such configurations are characterized by ring-like ribbons, brightenings running along them, and impulsive time-profiles.

Two compact regions denoted 1 and 2 in Figure 9b have a maximum brightness in the variance map which reveals their highest variability. The time-profiles computed over the whole jet and over the two compact regions 1 and 2 are shown in Figure 9c. They demonstrate that coronal region 1 and region 2 in the base of
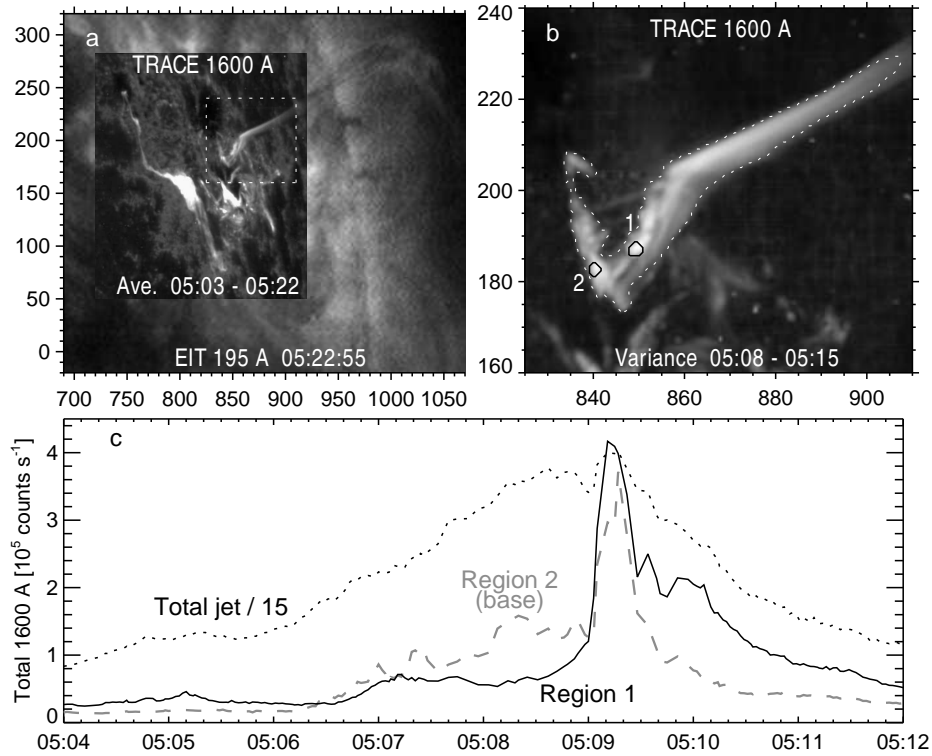
Figure 9. a) The overall configuration of the jet in an EIT 195 Å image combined with an averaged TRACE 1600 Å image (inset). A jet visible in 1600 Å occurred in a long loop-like structure visible in 195 Å. b) Enlarged variance map of the jet produced from the TRACE 1600 Å images during 05:08–05:15. The field of view corresponds to the white dotted frame in panel a. Labels 1 and 2 denote the regions, where a sharp brightening occurred. The axes in panels a and b indicate the distance from solar disk center in arcseconds. c) Time-profiles over the whole jet within the dotted contour (reduced by a factor of 15) and those of the small regions 1 and 2 denoted in panel b.

the jet exhibited a simultaneous brightening as short as 20 s, suggesting a sharp impulsive energy release at about 05:09. This pulse, the preceding collision of the flux rope with the separatrix surface of the funnel, and a pressure pulse produced in the bend of the long tube-like structure by the injected dense material of the jet results in a strong impulsive disturbance excited by the jet around 05:09. The shock-wave excitation by a similar jet-like eruption was demonstrated previously by Meshalkina *et al.* (2009) and Grechnev *et al.* (2011).

In summary, the whole event comprised three eruptions. The first eruption indicated by the first two-ribbon flare and a slowly-drifting radio burst occurred around 04:35. The second, main eruption associated with the fast CME occurred around 05:04. The third, jet-like eruption was actually observed around 05:09.

4. Drifting Radio Bursts

To find further information about the eruptions and shock wave in our event, we consider dynamic radio spectra in a wide frequency range. The structures visible in dynamic spectra reveal non-thermal electrons streaming along open magnetic fields (Type III bursts), tracing the fronts of shock waves (Type II bursts), or confined in quasi-static or expanding magnetic structures (Type IV bursts).

4.1. Type II Bursts

To analyze Type II bursts, we use our technique to outline their trajectory verified in studies of several events. The trajectory is governed by the plasma density distribution on the way of the propagating shock wave. A freely propagating blast-wave-like shock, which spends energy to sweep up the plasma with a radial power-law density falloff, $n(x) \propto x^{-\delta}$ (x is the distance from the eruption center), has a power-law kinematics, $x(t) \propto t^{2/(5-\delta)}$ *vs.* time t (Grechnev *et al.*, 2008b). The power-law density model, $n(h) = n_0(h/h_0)^{-\delta}$, with h being the height from the photosphere, $n_0 = 4.1 \times 10^8 \, \mathrm{cm}^{-3}$, $h_0 = 100 \, \mathrm{Mm}$, and $\delta = 2.6$ is close to the equatorial Saito model (Saito, 1970) at $h \geq 260 \, \mathrm{Mm}$, providing a steeper density falloff at lesser heights. The low-corona density increase corresponds to strongly disturbed conditions just before the appearance of the wave.

Thus, the expected trajectory of a Type II burst caused by the passage of the shock front through a structure with monotonically decreasing density is a gradual monotonic curve characterized by a steep onset and decreasing frequency drift. The wave onset time t_0 usually corresponds to the rise of the HXR or microwave burst or occurs earlier by up to two minutes. The degree of convexity of the trajectory is governed by the δ parameter, similarly to the influence of the exponent on the convexity of a power-law function.

Practically, we choose a reference point on the dynamic spectrum at time t_1, calculate a corresponding distance x_1 from our density model, and adjust t_0 and δ (typically $\delta \approx 2.5 - 2.9$) in sequential attempts to reach a best fit of the trajectory described by the equation $x(t) = x_1[(t - t_0)/(t - t_1)]^{2/(5-\delta)}$. We also use this approximation to fit different wave signatures such as "EUV waves" and leading edges of fast CMEs (Grechnev *et al.*, 2011, 2013a, 2014b, 2015b, 2016).

Figure 10 presents a combined dynamic spectrum composed from the *Hiraiso Radio Spectrograph* (HiRAS) spectrogram above 180 MHz and the Learmonth one below 180 MHz in Figure 10b, and the *Wind*/WAVES (Bougeret *et al.*, 1995) Rad2 receiver spectrogram in Figure 10d. For comparison Figure 10a shows the microwave burst at 17 GHz (NoRP: black) and 2.7 GHz (Learmonth: pink, late part only) as well as the total emission in 1600 Å from the west ribbon and jet (same as in Figure 6b). Since it is difficult to show all relevant features in a single image, we separately present in the inset in Figure 10c an enlarged part of the Learmonth spectrogram, whose actual position is denoted by the white frame.

The inset in Figure 10c reveals two pairs of narrow-band harmonic Type II lanes crossing each other. The $(1_\mathrm{F}, 1_\mathrm{H})$ pair outlined by the dotted lines is band-split. The $(2_\mathrm{F}, 2_\mathrm{H})$ pair outlined by the dashed lines has a faster frequency drift. Adjustment of the wave onset time (with an uncertainty within one minute)
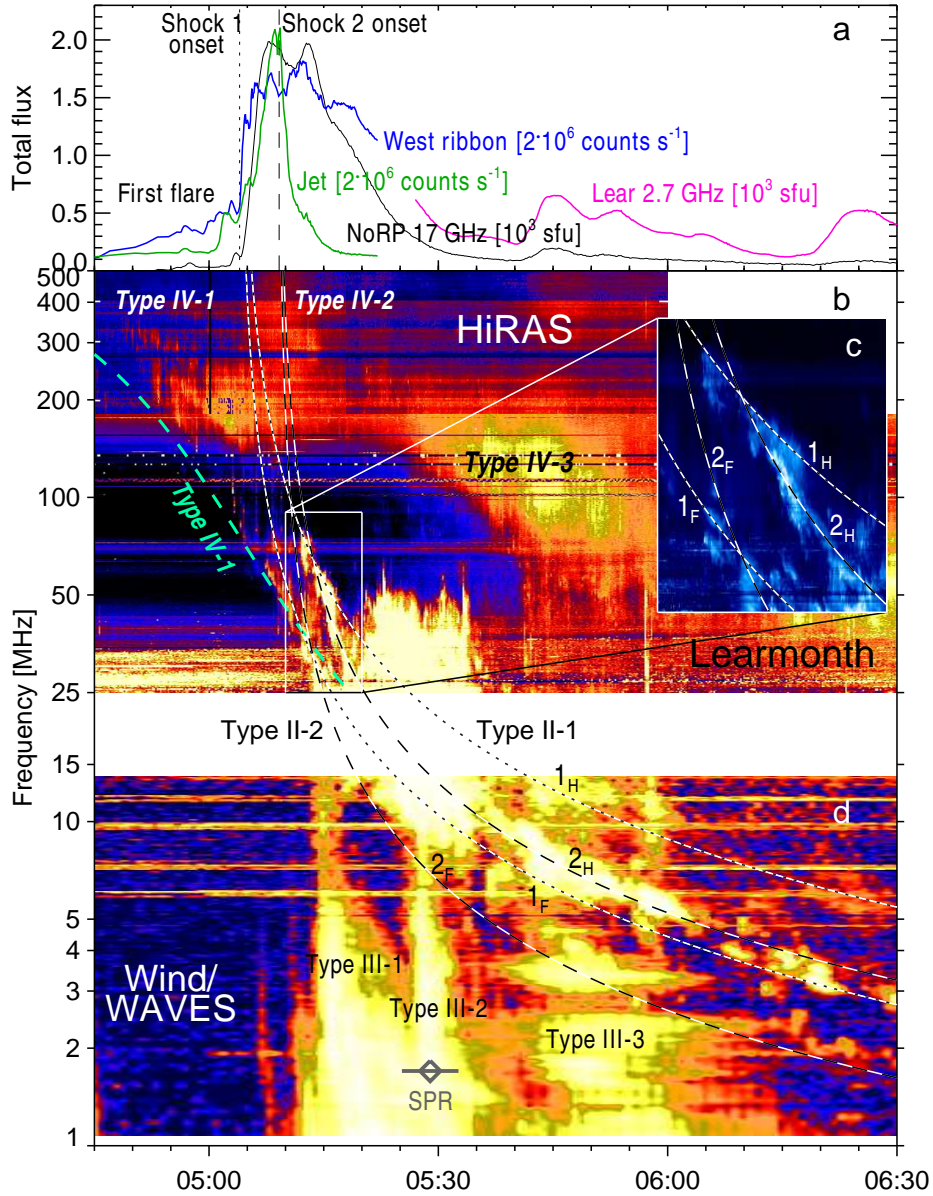
Figure 10. Combined dynamic spectrum (b and d) in comparison with the flare light curves (a). The vertical broken lines in panel a represent the onset times of shock 1 ($t_{01} = 05:04:00$) and shock 2 ($t_{02} = 05:09:10$). Inset c presents an enlarged part of the Learmonth spectrogram denoted by the white frame. The slowly drifting radio bursts are outlined with calculated trajectories. The dashed green curve (not shown in the inset) outlines the low-frequency envelope of Type IV-1 above 25 MHz. Traces of Type II-1 are outlined by the pair of dotted lines ($\delta_1 = 2.65$), and those of Type II-2 are outlined by the paired dashed lines ($\delta_2 = 2.54$). The gray diamond at the bottom labeled SPR denotes the estimated SPR time with an uncertainty represented by the gray bar (Reames, 2009b).
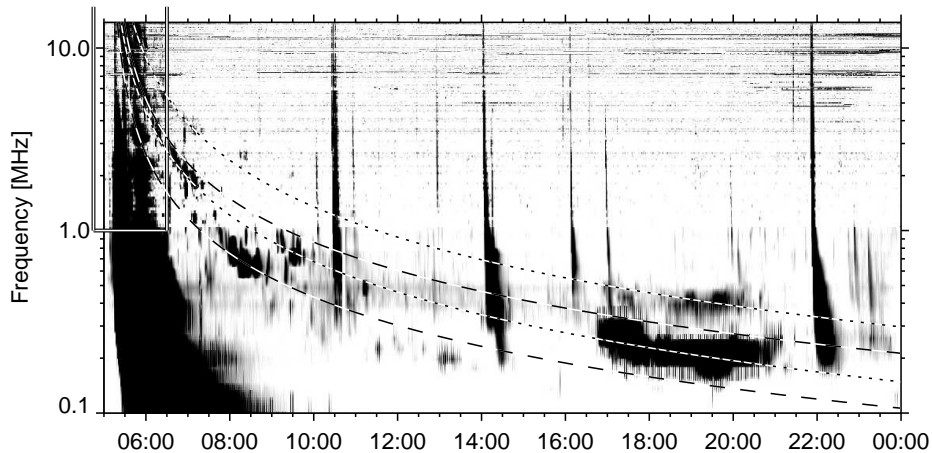
Figure 11. Interplanetary Type II event in a *Wind*/WAVES Rad2 + Rad1 spectrogram (adapted from Cane and Erickson (2005)). The pairs of dotted and dashed curves, same as in Figure 10, outline the trajectories of two shock waves following each other. The white-on-black frame represents the range shown in Figure 10.

and density falloff exponent for each of the two pairs of bands has shown that they were caused by two different shock waves following each other. The first shock wave started at $t_{01} = 05{:}04{:}00$ and was caused by the main eruption (*cf.* Figure 10a). The second shock wave ($t_{02} = 05{:}09{:}10$) was produced by the jet. The difference in the density falloff exponents ($\delta_1 = 2.65$ *vs.* $\delta_2 = 2.54$) suggests that Type II-1 and Type II-2 were emitted from different coronal structures.

Continuations of the trajectories to the frequencies $< 25\,\mathrm{MHz}$ are not obvious because of the gap between the HiRAS & Learmonth and *Wind*/WAVES bands as well as the complex structure of the Type II bursts. Therefore, the identification of the bands in the *Wind*/WAVES spectrogram is not guaranteed, while the calculated trajectories match the actual evolution of the frequency drift. The *Wind*/WAVES spectrogram shows, at least, three Type II bands, confirming the presence of two shocks. Two shock waves following each other within a few minutes were observed previously (Grechnev *et al.*, 2011, 2013a).

The Type II emission in this event was observed up to very low frequency of about $150\,\mathrm{kHz}$. It is a long-standing issue if Type II emissions observed in the decametric/hectometric (DH) range and at still longer waves, also termed interplanetary (IP) Type II events, can be extensions of metric Type II bursts. An apparent mismatch between the trajectories of the former and latter events has been considered as an indication of different origins of the responsible shocks.

In this view, Cane and Erickson (2005) examined several events and estimated that '$< 15\,\%$ of the Type IIs extending below $15\,\mathrm{MHz}$ actually extend below $5\,\mathrm{MHz}$ and that the lowest frequency extent is about $1\,\mathrm{MHz}$'. The authors found 'no clear example of a metric Type II burst that extends continuously down in frequency to become an IP Type II event' at lower frequencies. The 2001 December 26 event was specially considered by the authors with a conclusion 'like other events, there is a disjoint in frequency between the Type II burst and emission likely to be related to the CME shock [*i.e.* IP Type II event]'.

To understand if our analysis can shed light on this problem, we extend our outline of the two shock waves from Figure 10 up to 100 kHz. Because Cane and Erickson (2005) were concerned about a proper frequency scaling of concatenated spectrograms (here *Wind*/WAVES Rad2 + Rad1), we have taken their Figure 13 and plotted over it our trajectories found from the metric Type II bursts without any additional adjustment. The result is shown in Figure 11. The white-on-black frame in the top-left corner denotes the field of view in Figure 10.

Although the Type II bands are not continuous and their identification is not guaranteed, the calculated trajectories correctly reproduce the actual evolution of the frequency drift throughout the event in the whole frequency range. There is no mismatch between the metric and IP Type II emission. The impression about the mismatch was probably due to a complex structure of the radio emission with gaps between observed Type II portions and presence of misleading features, which are probably irrelevant to the main trajectories.

Figure 11 also leads to the following conclusions. i) The Type II emission in the whole range where it was observed, from about 80 MHz to about 150 kHz was due to the same shock wave, which was excited by the eruption in AR 9742 during the flare. ii) The Type II bands and blobs in the $0.5 - 5$ MHz range between 06:30 and 10:00 corresponding to different dotted and dashed trajectories certify the presence of two different sources of the Type II emission. This fact rules out a popular idea relating the Type II source to the bow-shock ahead of the CME nose. At least, one of the radio sources must be located at a flank of the shock wave, because two bow-shocks cannot be driven by a single piston. Most likely, two lateral blast-wave-like shocks coexisted, at least, until 09:00, while ahead of the CME they merged into a single stronger shock (Grechnev *et al.*, 2011).

4.2. Type IV Bursts

A slowly-drifting burst visible in Figure 10b from 04:50 until 05:13 outlined from below by the dashed green line resembles a Type II burst. So it was reported by some observatories and considered by Nitta *et al.* (2012). However, the trajectory of this burst with an increasing drift rate looks oppositely to those of Type II-1 and Type II-2. The structure of this burst is better visible in Figure 12, which presents an adapted HiRAS spectrogram (2001122605.gif) accessible at sunbase.nict.go.jp/solar/denpa/hirasDB/Events/2001/.

At the first glance, the burst consisted of a pair of bands with a frequency ratio of 1.8 (the bright red feature visible from 05:12 to 05:16 between 40 and 80 MHz is due to Type IIs). Its frequency spectrum is clearly cut off towards lower frequencies, as expected for a population of confined electrons. The high-frequency cutoff has a less pronounced drift, if any, so that the bandwidth of this burst increases. This looks like a Type IV burst and not like a Type II. This burst, which we call Type IV-1, was probably due to emission from an electron population confined in an expanding magnetic structure.

The second burst in Figure 12 started since about 05:05 in association with the main eruption. Because of its broad bandwidth this is probably also a Type IV burst (Type IV-2). Its quasi-stationary high-frequency part extending up to > 2000 MHz lasted until about 05:27, being probably related to the flare
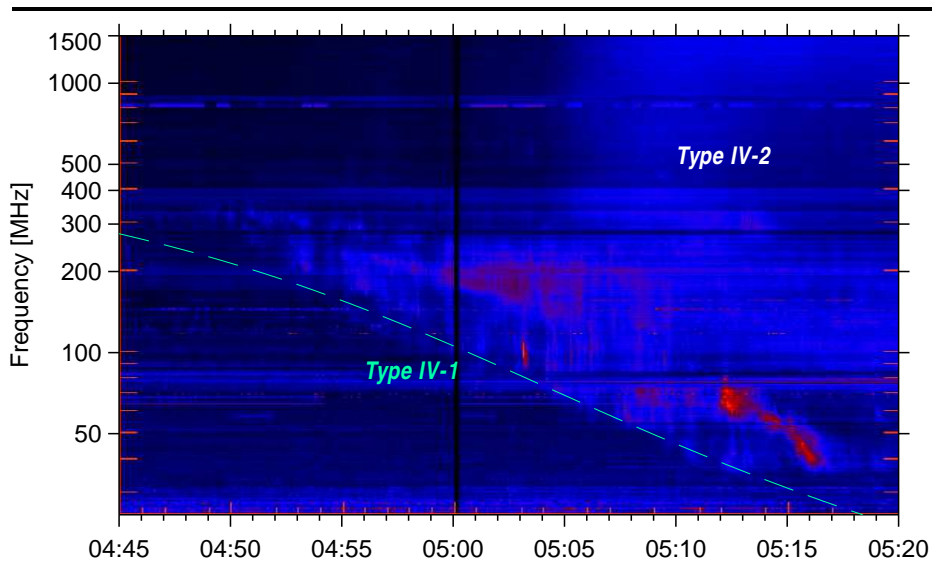
Figure 12. Type IV bursts in the HiRAS spectrogram. The dashed green curve (same as in Figure 10b) outlines the low-frequency envelope of the burst corresponding to the height–time plot in Figure 13a.

arcade. The HiRAS spectrogram suggests a drift of its low-frequency part to lower frequencies (invisible in Figure 10b). One more slowly-drifting Type IV-3 burst superposed on a Type III group is visible in Figure 10b considerably later, being probably due to emission from the structures well behind the CME leading edge. It is difficult to analyze Type IV-2 and Type IV-3 because of their poor appearance and overlap with different structures.

We focus on Type IV-1. This slowly drifting burst evidences the presence of a moving source. The moving radio source is really often observed along the extrapolated trajectory of an erupting prominence (see, *e.g.*, McLean, 1973; Klein and Mouradian, 2002). By relating a drifting Type IV burst to the simultaneous expansion of an SXR source, Grechnev *et al.* (2014b) reconstructed its kinematics in a time interval exceeding imaging observations. The approach is as follows.

The lowest instantaneous frequency of a radio burst is determined by the plasma frequency $f_{\mathrm{P}} \approx 9 \times 10^3 n^{1/2}$ in an emitting volume. Assuming the frequency drift to be due to the density decrease in an expanding volume characterized by a size r and relating the low-cutoff frequency to the plasma frequency, $f_{\mathrm{p}} \propto n^{1/2} \propto r^{-3/2}$, it is possible to infer the kinematics of the corresponding magnetic structure by adjusting the low-frequency envelope of the Type IV burst (Grechnev *et al.*, 2014b). An additional indication is an expected similarity of the velocity–time plot of the eruption to the SXR flux (Zhang *et al.*, 2001; Grechnev *et al.*, 2014b, 2016). To find an uncertain multiplier relating the spatial and frequency (density) scales, we refer to the top of the first eruption revealed by the EIT images in Figure 7. These plane-of-the-sky measurements are corrected for the longitude of the active region $\lambda = 54°$ by applying a factor of $1/\sin\lambda$.

We composed the acceleration time-profile from two Gaussian pulses, adjusting their parameters to make the antiderivative similar to the SXR flux and
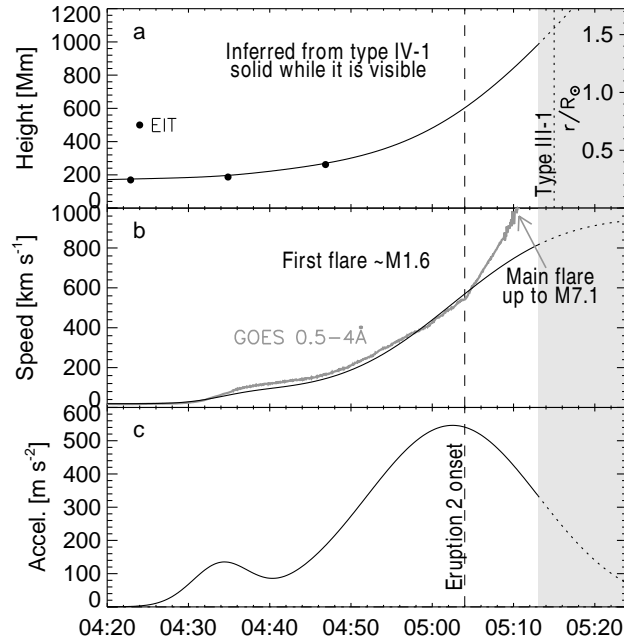
Figure 13. Kinematics of the first eruption (leading edge) in the radial direction inferred from the analysis of the Type IV-1 burst, SXR flux, and EIT data (filled circles, Figure 7). a) Height–time plot. b) Velocity–time plot along with a GOES SXR flux scaled to match the velocity. c) Acceleration–time plot. The shading denotes the interval when Type IV-1 is no more discernible. The dashed vertical line denotes the onset time of the second eruption. The dotted vertical line in panel a denotes the onset time of the Type III-1 burst.

to reproduce the Type IV-1 envelope (see Grechnev *et al.*, 2011, 2013a, 2014b, 2016 for the description of the technique). The inferred kinematical plots are presented in Figure 13, and the calculated low-frequency envelope of Type IV-1 is shown in Figures 10b and 12 by the dashed green line. The correspondence of the inferred kinematics to the Type IV-1 burst, SXR flux, and the measurements from EIT data confirms its likelihood. In spite of remaining uncertainties, it is clear that when the second eruption started, the first erupting structure has reached a considerable height of about 600 Mm, being still not far away. It stretched closed loops ahead of the main erupting structure, cleared away the path for its expansion, and thus facilitated its lift-off.

4.3. Type III Bursts

The *Wind*/WAVES spectrum in Figure 10d shows three strong Type III bursts. Type III-1 started at the high-frequency edge of the Rad2 passband around 05:15 and lasted within three minutes. Type III-2 started around 05:27 and had a similar duration. No metric Type III bursts are detectable before Type III-2. Conversely, Type III-3 corresponds to a clear group of metric Type IIIs in an interval of 05:40 – 06:00, when minor microwave bursts are visible at 17 GHz in Figure 10a. The sources of these bursts were also located in AR 9742 (Article I).

While production of accelerated electrons in the flare region is evidenced by the flare emissions in the whole interval of Figure 10a, the absence of metric Type IIIs until Type III-3 indicates confinement of the magnetic configuration in AR 9742 and its isolation from the magnetic fields open into the interplanetary space. Importance of two short, weak Type IIIs in Figure 10d before Type III-1 is doubtful. The configuration clearly became opened, when Type III-3 started.

Type III-1 has no extension in the metric range, being unlikely due to escape of electrons from the flare region. Its starting frequency is between 14 and 25 MHz. The only apparent source of non-thermal electrons to produce Type III-1 is the expanding flux rope, which appeared in the first eruption and contained trapped electrons responsible for Type IV-1. Reconnection between this flux rope and an open magnetic structure like a streamer (Grechnev *et al.*, 2013a) or coronal hole (Masson, Antiochos, and DeVore, 2013) could create a path, along which electrons trapped in the flux rope escaped into the interplanetary space (Aschwanden, 2012). Besides electrons, protons and heavier ions, both pre-existing in the flux rope and injected into it in the course of flare reconnection, from thermal and suprathermal up to accelerated to high energies, were released. These particles supplied a rich seed population for acceleration by a trailing shock wave. The presence of the Type IIIs in the whole frequency range of *Wind*/WAVES shows that the particles released could reach the Earth orbit.

The onset time of Type III-1 denoted by the vertical dotted line in Figure 13a corresponds to a height of the flux-rope's leading edge of $\approx 1.55 R_\odot$. A probable site of reconnection between the flux rope and a static open magnetic structure (streamer or coronal hole) is at a farthest edge of the flux-rope's flank, approximately at a height of $0.78 R_\odot$ for a circular geometry. The plasma frequency expected at this height is 30 MHz in a streamer (Newkirk, 1961) and 8.6 MHz in a coronal hole (Saito, Poland, and Munro, 1977) *vs.* expected $14 - 25$ MHz. With uncertainties we have, either option is possible.

Although the height–time plot of the second flux rope formed in the main eruptive flare is not known, there are indications of a similar scenario related to Type III-2. These are the appearance just after the main flare onset of Type IV-2 and its probable drift to lower frequencies; the starting frequency of Type III-2 between 9 and 25 MHz, similar to that of Type III-1, without extensions into the metric range; and a probable opening of the magnetic configuration associated with Type III-2. The second flux rope reconnected with the same open magnetic structure as the first one and at a comparable height.

The particles accumulated in the second flux rope in the course of the much stronger main flare were released after the Type III-2 onset. This second population of released particles is expected to be more energetic and plentiful. The estimated SPR time (Reames, 2009b: the gray diamond labeled SPR) coincides with Type III-2. The first particle release in association with Type III-1 does not contradict the GLE onset 12 minutes earlier than the estimated SPR time (the dashed line in Figure 2b), so that a direct contribution to the SEP event from particles accelerated in the first flare is also possible.

Type III-3 indicates direct escape of electrons (and probably other particles) from the flare region evidenced by a dense group of the corresponding metric
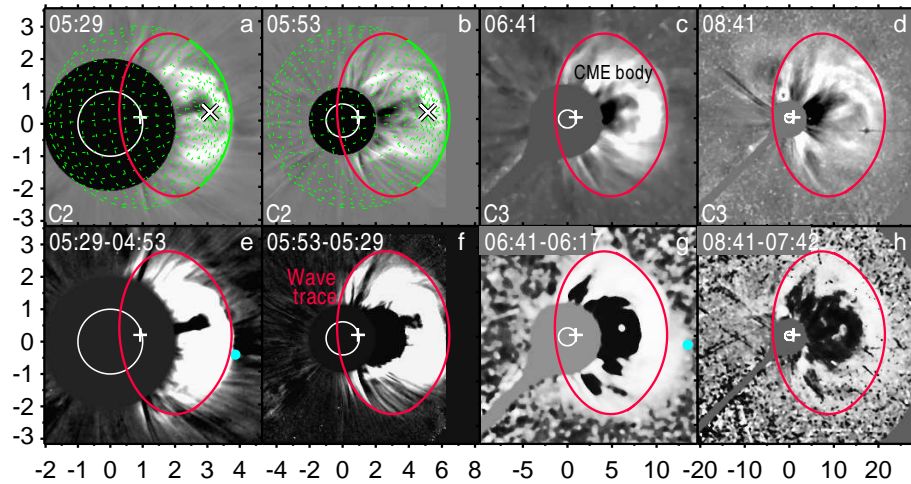
Figure 14. CME body (top) and wave traces (bottom, running differences) in LASCO/C2 and C3 images. Panels a and b explain the calculations of the wave outline (red in other panels). A bulge protruding southwest is visible in later images. The blue filled circles in panels e and g denote the measurements in the CME catalog corresponding to the bulge. The axes indicate the distance from solar disk center in solar radii.

Type IIIs. The peak of the microwave spectrum shifted from about 6 GHz (Article II) to ≈ 2.7 GHz at that time, as comparison of the microwave burst at 17 GHz (black) and 2.7 GHz (pink) in Figure 10a shows. This suggests displacement of the microwave-emitting region (and, possibly, the site of the flare energy release) to weaker magnetic field at larger altitudes. These late-stage processes can be related to the post-impulsive particle acceleration (see, *e.g.*, Chertok, 1995; Klein *et al.*, 1999, 2014). The possibility to accelerate the released population of particles by the shock wave is questionable.

5. White-Light CME

A white-light transient was observed by the LASCO C2 and C3 coronagraphs starting from its appearance at 05:29 up to the outer edge of the C3 field of view at 30R$_\odot$. The transient consisted of a structured CME body (probable flux rope) surrounded by a fainter partial-halo wave trace. The same LASCO images in Figure 14 processed in different ways reveal CME structures (top) and partial-halo wave traces (bottom, running differences). The wave traces are detectable from a diffuse halo-like brightening or deflected coronal rays (the latter are conspicuous in Figure 14f).

The sky-plane expansion of the CME body and wave was very similar. We therefore fitted the kinematics of both with the same power-law fit appropriate for a shock wave. The wave onset time, $t_0 = 05{:}10{:}00$, is slightly later than that of shock 2 ($t_{02} = 05{:}09{:}10$), corresponding to the fact that two shock waves propagating away from the Sun one shortly after another should merge in the frontal direction into a single stronger shock wave with an apparently later onset
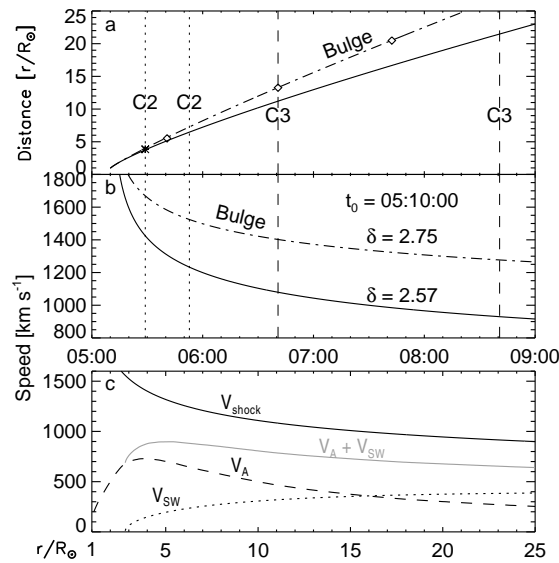
Figure 15. Kinematic plots of the transient visible in LASCO images. a) Height–time plots for the main envelope of the CME leading edge (solid) and for the bulge (dash-dotted). The symbols represent the measurements from the CME catalog. b) Speed–time plots for the main CME envelope (solid) and the bulge (dash-dotted) calculated for a decelerating shock wave with the same onset time, $t_0 = 05:10:00$, but with different density falloff exponents δ. c) Distance–velocity plot for the main CME envelope (black solid) corresponding to the wave along with the models of the Alfvén speed V_A (dashed) and solar wind speed V_{SW} (dotted) above the quiet Sun. The gray curve represents the sum $V_A + V_{SW}$.

time (Grechnev *et al.*, 2011). The power-law exponent is $\delta = 2.57$, close to the mid-latitude Saito model. The kinematical plots are shown in Figures 15a and 15b by the solid lines. Using this kinematics, the images in Figure 14 are progressively resized to maintain the visible size of the expanding transient (see also the 2001-12-26_LASCO.mpg movie in the electronic version of the article).

Figures 14a and 14b explain how the shape of the wave front was calculated. Green is a sphere centered at the eruption site (straight cross), with a polar axis extending its radius-vector (slanted cross marks the pole), and a radius taken from Figure 15a. Red is a small circle on this sphere. The closed red curve in the other panels of Figure 14 composed from the red and green arcs in Figures 14a and 14b matches most wave traces in all images. Thus, the main part of the wave front is a conic section of the sphere, what is expected for a spherical blast wave. The deflected rays outside of the outline in Figure 14e are most likely due to the flanks of the earlier shock 1 ($t_{01} = 05:04$). Traces of two shock waves propagating one shortly after another across the solar disk up to the limb were demonstrated previously by Grechnev *et al.* (2013a).

Figure 14g also reveals a southwest bulge ahead of the red outline. The bulge might seem to be a manifestation of the bow-shock; however, its orientation is offset from the main expansion direction of the CME. On the other hand, correspondence of the orientation of the bulge to the position of a large coronal hole in Figure 4 indicates that the bulge was caused by the fast solar wind stream

originating in the coronal hole. The measurements in the online CME catalog (cdaw.gsfc.nasa.gov/CME_list/: Yashiro *et al.*, 2004) are related to the bulge. They are denoted by the symbols in Figure 15a and outlined in Figures 14a and 14b by the power-law fit with a steeper density falloff exponent of $\delta = 2.75$ expected for a coronal hole.

Figure 15c presents the velocity *vs.* distance plot (black solid) of the main CME envelope corresponding to the spherical wave front (without the bulge). This is a power-law fit for the apex of the observed wave front. For comparison, the dashed curve represents the model for the Alfvén speed, V_A, above the quiet Sun (Mann *et al.*, 2003). The dotted curve represents the model for the solar wind speed, V_{SW} (Sheeley *et al.*, 1997). If the wave intensity were very small, then the velocity of its motion would be $V_{SW} + V_{fast}$ with V_{fast} being the fast-mode speed. The heading part of the wave front moves at distances $(5-25)R_\odot$ practically along the magnetic field, *i.e.* $V_{fast} \approx V_A$ (with V_A exceeding the sound speed). Considerable excess over the Alfvén speed of the wave speed relative to the moving environment $V_{shock} > V_A + V_{SW}$ (the sum is shown by the gray curve) certifies the shock-wave regime in the whole range of distances. The wave intensity characterized by the Mach number can be estimated as $M = (V_{shock} - V_{SW})/V_A$ (with an increasing M this formula becomes inaccurate). The Mach number is $M \approx 1.6$ at distances $(5-10)R_\odot$, whereas $M \approx 2$ at $25R_\odot$.

In summary, the partial halo surrounding the CME body was most likely due to the shock wave, which had both blast-wave and bow-shock properties in the LASCO field of view, from $3.8R_\odot$ to $30R_\odot$. The CME and wave were super-Alfvénic and expanded similarly (bow-shock), while their common kinematics and the spherical wave front corresponded to the impulsively-excited blast wave, whose propagation was controlled by the growing mass of the swept-up plasma.

6. Discussion

6.1. Presumable Kinematics of the Fast CME

The results of the analysis allow reconstructing presumable kinematics of the fast CME. We also invoke the following conclusions and observational results: i) acceleration of a CME is synchronous with an HXR (or microwave) burst (Zhang *et al.*, 2001; Temmer *et al.*, 2008, 2010; Grechnev *et al.*, 2015b); ii) the velocity–time plot of a CME is similar to the SXR flux (Zhang *et al.*, 2001; Grechnev *et al.*, 2016); iii) the Neupert effect: the time-profile of an HXR (microwave) burst is similar to the derivative of the SXR flux (Neupert, 1968); and iv) the height–time and velocity–time plots of the CME in the LASCO field of view should be close to those of the shock wave in Figures 15a and 15b (Section 5).

According to the last item, the initial impulsive acceleration of the fast CME should be followed by a deceleration phase, because the shock wave decelerated all the time. We therefore composed the CME acceleration as a positive Gaussian pulse resembling the microwave burst followed by a negative pulse. The velocity should be roughly similar to the GOES $1-8$ Å flux, being about $1000\,\mathrm{km\,s^{-1}}$ at 07:30. The result is shown in Figure 16 by the dashed curves. The dotted curves
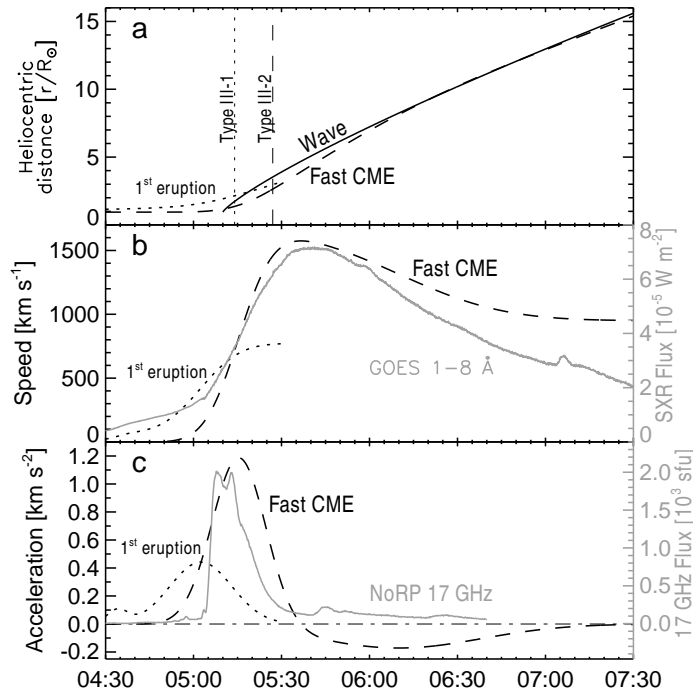
Figure 16. Presumable plane-of-the-sky kinematics of the fast CME (dashed) up to 15R$_\odot$ inferred from indirect indications. a) Distance–time plot and a wave plot from Figure 15a (solid). b) Velocity–time plot along with a GOES SXR flux (gray). c) Acceleration–time plot and a microwave burst at 17 GHz (gray). The dotted curves correspond to the first eruption (Figure 13) inferred from the analysis of Type IV-1 and corrected to the plane of the sky. The broken vertical lines in panel a denote the onset times of the Type III-1 and Type III-2 bursts.

correspond to the first eruption (Figure 13 in Section 4.2) corrected to the plane of the sky by a factor of $\sin\lambda$ (with a longitude $\lambda = 54°$). The CME and shock wave (solid lines) in Figure 16a are close to each other after 05:30, as expected.

The presence of two eruptions forming the CME complicates the situation. The flux rope ejected during the first flare eventually constituted the CME top part and the second flux rope joined it from below. The difficulties to untangle the kinematical plots of the two CME components result in the differences between the CME speed and SXR flux in Figure 16b and between the CME acceleration and microwave flux in Figure 16c. The derivative of the SXR flux, which contains an increasing component from the first flare, is smoother than the 17 GHz burst. We have adopted a compromise shape of the acceleration somewhat smoother than the microwave burst and a corresponding velocity somewhat sharper than the SXR flux. The estimated acceleration peak (1.2 km s^{-2} in the plane of the sky and 1.5 km s^{-2} in the radial direction) is comparable with a radial acceleration of 1.1 km s^{-2} estimated by Gopalswamy *et al.* (2012) for this event from different considerations. Our value might be still underestimated; nevertheless, the plots appear to be acceptable with uncertainties we have.

The CME plots in Figure 16 were reconstructed on the basis of recent results by referring to dynamic radio spectra and scarce imaging observations. These presumable plots lead to the following conclusions discussed in the next sections.

1. The acceleration of second flux rope corresponds to a typical impulsive piston. It must have excited a blast-wave-like shock not later than the acceleration peak. The second flux rope was below the first one at that time.
2. The second flux rope exceeded the first one in speed and acceleration by a factor of ≥ 2 and became super-Alfvénic before its observations by LASCO.
3. The heights reached by the first flux rope and the second one, when corresponding Type III bursts started, are comparable, being related as 1:1.35.

6.2. Shock Wave

6.2.1. Shock-Wave History

The pieces of the observational material found for this event fit within a scenario outlined in Section 1. The second flux rope formed by reconnection also responsible for the flare, accelerated and produced a strong disturbance, as an impulsive piston. The shock-wave excitation by the jet-like eruption is similar. The impulsive-piston scenario is well known – see, *e.g.*, Vršnak and Cliver (2008). A crucial factor for the shock formation not considered in this review is inhomogeneous distribution of the fast-mode speed. Propagating into environment of a much lower fast-mode speed, the disturbance undergoes jam of its profile and must rapidly steepen into the shock (Afanasyev, Uralov, and Grechnev, 2013).

The impulsive-piston excitation of the shock wave and its properties resemble the expectations for the hypothetical ignition of a freely propagating decelerating blast wave by the flare pressure pulse. However, the role of the impulsive piston in the observed events is played by the erupting flux rope rather than the flare loops. The flare-ignition of shock waves is neither supported by observations nor expected from general considerations for the following reasons.

The plasma pressure in flare loops is controlled by its temperature and density, which also determine their SXR emission. It is intrinsically gradual and usually resembles the antiderivative of the HXR or microwave burst (the Neupert effect: Neupert, 1968). On the other hand, the HXR burst is similar to the acceleration pulse of an erupting structure, as several studies concluded (see Section 1). Thus, an erupting structure produces a generally much sharper pulse of the pressure than its gradual increase in flare loops, being a more efficient impulsive piston.

Even if the plasma beta in flare loops reaches $\beta \sim 1$, then this is a normal situation in a flare. The plasma pressure in flare loops increased due to chromospheric evaporation is balanced by the dynamic pressure of the reconnection outflow. All dimensions of a flare loop should increase by an inconsiderable factor of $\sqrt[4]{1+\beta}$ (Grechnev *et al.*, 2006). The disturbance would be too weak to ignite a shock wave. Our observational studies have shown that the size of an SXR-emitting region associated with flare loops does not change, when the shock wave appears, and its onset time is close to the acceleration peak of an erupting structure, which can precede the HXR peak by $1-2$ minutes.

We found that the shock waves were impulsively excited by sharply erupting flux ropes in eight events, where their kinematics was measured. These events range from the GOES B class to the X class and were or were not accompanied by non-thermal bursts in HXR and/or microwaves. The shock waves in these events, as well as three others, in which their exciters were not measured, demonstrated identical behaviors, initially resembling blast waves. In the events with fast CMEs, the shock waves exhibited some properties of the bow shocks only after some time, changing from the blast-wave-like regime to the bow-shock-like one. The pure bow-shock excitation scenario has not been found in any of flare-related eruptions. Two shock waves following each other within six minutes observed in two events rule out their bow-shock regime presumed in most studies of SEPs (Reames, 2009a; Aschwanden, 2012; Gopalswamy *et al.*, 2012; and others). Its initial appearance is not excluded for gradually accelerating non-flare-related CMEs caused by eruptions of huge quiescent filaments.

The 26 December 2001 event associated with a major flare shows the same shock-wave history as a number of flare-related events studied previously. The first shock wave was impulsively excited by the main eruption at 05:04. The second, similar one was excited by the jet at 05:09. Both shock waves initially resembled decelerating blast waves and followed each other for some time. The trailing front must have reached the leading one around the radial direction, so that the two shocks merged into a single stronger one with an apparently later onset time. As concluded in Section 5, the partial halo surrounding the CME body was a trace of a shock wave, whose properties in the LASCO field of view were intermediate between the blast wave and bow shock.

6.2.2. Regimes of Shock Waves

The solid curve in Figure 15c, being a power-law fit of the measured shock-wave speed, formally corresponds to a solution of a self-similar blast wave in a medium with a power-law dependence of the density on the distance. The mass of plasma involved in the motion continuously grows. The integral of the kinetic energy is conserved, as well as the integral of the sum of the plasma thermal energy and magnetic field energy within the volume behind the shock front. Conservation of both energy integrals in this regime means a continuously increasing impulse of the mass moving within a fixed solid angle, if the density falls off not steeper than r^{-3} (to have an initial mass finite). The increase of the impulse is caused by a significant pressure difference upstream and downstream of the shock front. The system consisting of the CME and associated shock possesses such properties. The initial impulse of the system is zero, the total mass of the moving gas grows, and the impulse increases due to magnetic driving forces responsible for the development and expansion of the CME. This situation persists up to some distance. Our power-law fit applies to the position and speed of the decelerating shock front at this stage.

The magnetic driving forces responsible for the CME impulse increase at the first stage weaken, as the distance from the Sun increases. The outer magnetic influence on the CME and disturbed solar wind ceases. The total impulse of this system starts conserving. The CME deceleration is governed by the regime of

the CME interaction with the solar wind. Two extreme regimes are possible: i) flow around the CME without change in its mass, and ii) the 'snowplough' regime, when the mass of the CME moving by inertia at this stage keeps on growing because of adhesion of the solar wind plasma to the CME instead of flowing around it. The change in the CME impulse in either regime is equal (but opposite) to that of the solar wind. The total drag force is equal to the time-derivative of this impulse and can be calculated. We do not consider the 'snowplough' regime, which results in a considerably stronger deceleration than the solid curve in Figure 15c shows. The mass increase is unlikely at large distances from the Sun, where the CME expands radially.

Two situations of the flow around the CME are possible: i) the solar wind flow rapidly recovers behind a compact CME, and ii) the disturbed zone behind the CME is much larger than that ahead it. The drag force of the solar wind is absent in the idealized first situation and is largest in the second one. If the difference between the velocities of the CME leading edge and solar wind, $V_{\mathrm{CME}} - V_{\mathrm{SW}}$, exceeds the fast-mode speed ahead the CME, V_{fast} (as was the case in our event), then bow shock exists ahead of the CME with a speed practically equal to V_{CME}.

A model of the stationary solar wind is usually invoked to calculate V_{fast}. In a real situation, the CME formation is associated with the appearance of a large-scale fast-mode shock wave. Propagating up like a blast wave, it leaves behind an extended region, where V_{fast} is higher than the calculated value, so that $V_{\mathrm{CME}} - V_{\mathrm{SW}} < V_{\mathrm{fast}}$ for some time. The CME expansion at this stage has a character of a flow and bow shock is absent.

After that, bow shock can appear even during the early CME expansion, but its role is insignificant, as long as the driving forces surpass the drag force. Only after the driving forces diminish relative to the drag force, the latter dominates the CME kinematics. Deceleration of both a freely propagating blast wave and bow shock ahead of a fast CME influenced by the aerodynamic drag complicates identification of the shock-wave regime. To assess the role of the drag at different distances, we will compare the observed velocity–distance plot with expectations for the bow-shock regime. The $V_{\mathrm{CME}}(t)$ dependence necessary for the calculations of the bow-shock curves was found from the motion equation

$$m_{\mathrm{CME}}(\mathrm{d}V_{\mathrm{CME}}/\mathrm{d}t) = -\rho(V_{\mathrm{CME}} - V_{\mathrm{SW}})^2 S \equiv F_{\mathrm{drag}}, \tag{1}$$

where $m_{\mathrm{CME}} = \mathrm{const}$ and S are the effective mass of the CME and its cross-section. At a sufficient distance $S \propto r^2$. For simplicity we take V_{SW} at a reference distance r_{ref}, neglecting its gradual variation in Equation (1). Due to conservation of a plasma flow in stationary solar wind with a density ρ, $\rho S = \rho_{\mathrm{ref}} S_{\mathrm{ref}} = \mathrm{const}$. The 'ref' subscript corresponds to a distance r_{ref} or a time t_{ref}. We transform Equation (1) to a form

$$\mathrm{d}V_{\mathrm{CME}}/\mathrm{d}t = -C(V_{\mathrm{CME}} - V_{\mathrm{SW}})^2, \tag{2}$$

with $C = \rho_{\mathrm{ref}} S_{\mathrm{ref}}/m_{\mathrm{CME}}$. Solution of Equation (2) is a function

$$V_{\mathrm{CME}} = V_{\mathrm{CME}}(t_{\mathrm{ref}}) \left(1 + \kappa_{\mathrm{ref}} \frac{t - t_{\mathrm{ref}}}{\tau_{\mathrm{ref}}}\right) \left(1 + \frac{t - t_{\mathrm{ref}}}{\tau_{\mathrm{ref}}}\right)^{-1} \tag{3}$$
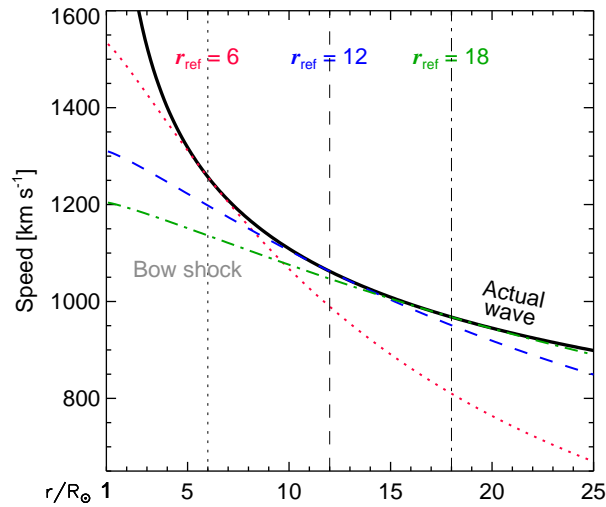
Figure 17. Comparison of the actual distance–speed wave evolution (same as in Figure 15c) with the plots expected for the bow-shock regime with different parameters (color curves). The broken vertical lines mark the reference distances $r_{\rm ref}$, at which the speed and deceleration of the actual wave were taken to calculate corresponding plots for the bow-shock regime (denoted by the same colors and line styles).

with $\kappa_{\rm ref} = V_{\rm SW}/V_{\rm CME}(t_{\rm ref})$, deceleration time scale $\tau_{\rm ref} = [C(V_{\rm CME}(t_{\rm ref}) - V_{\rm SW})]^{-1} = -[V_{\rm CME}(t_{\rm ref}) - V_{\rm SW}]/a_{\rm ref}$, and acceleration at a reference point $a_{\rm ref} = (F_{\rm drag}/M)_{t=t_{\rm ref}} = [{\rm d}V_{\rm CME}/{\rm d}t]_{t=t_{\rm ref}}$. The characteristic deceleration time $\tau_{\rm ref}$ is obtained by differentiation of Equation (3):

$$\tau_{\rm ref} = (\kappa_{\rm ref} - 1)V_{\rm CME}(t_{\rm ref})/[{\rm d}V_{\rm CME}/{\rm d}t]_{t=t_{\rm ref}}. \tag{4}$$

Figure 17 illustrates how the changing relation between the driving forces and drag force affects the CME deceleration. The black solid line is a power-law fit of the observed velocity *vs.* distance dependence for the shock wave. The broken color curves represent the trajectories $V_{\rm CME}(r)$ calculated by using Equations (3) and (4) under assumption of the constancy of the CME mass. Each curve for the bow-shock regime was calculated by referring to the velocities of the shock and solar wind at three reference distances $r_{\rm ref} = [6, 12, 18]{\rm R}_\odot$. Drag is formally assumed to dominate at points $r_{\rm ref}$, and the velocity of the shock-wave front is equal to the CME speed, $V_{\rm shock} = V_{\rm CME}$, *i.e.* the wave is bow shock. If the drag force surpassed the driving forces in the whole range of distances, then all the four curves in Figure 17 coincided. In reality, the calculated curve approaches the experimental plot only at distances $r \geq r_{\rm ref} \approx 15{\rm R}_\odot$, where aerodynamic drag can determine the CME deceleration.

6.2.3. Interplanetary Type II Event

A new finding is consistency of a predicted Type II trajectory with observations up to very low frequency of about 250 kHz (Figure 11). This result reconciles the Type II emissions in the metric range with longer waves and addresses a

long-standing discussion over their seemingly different origins (*e.g.* Cane and Erickson, 2005). Some other properties of the IP Type IIs become clearer.

A narrow-band Type II emission can only appear from a compact source in a distinct narrow structure like a coronal ray (Uralova and Uralov, 1994; Reiner *et al.*, 2003); otherwise, a drifting continuum is expected from a large-scale shock front crossing a wide range of plasma densities (Knock and Cairns, 2005). Coexisting signatures of two shocks in the Type II emission, at least, until 09:00 (Section 4.1) point at a location of, at least, one of their sources at a flank of the shock wave. On the way to an observer, the emission crossing the dense heliospheric plasma sheet can be subjected to refraction, interference, and/or absorption. The IP Type II emission from a moving compact source can temporarily fade and reappear producing a 'blobs and bands' structure (Cane and Erickson, 2005). The time structures of the IP Type IIs observed from the vantage points of *Wind* and STEREO can therefore be different.

6.3. Particle Release

6.3.1. Type III Bursts and Particle Release

Although remote-sensing methods for protons and heavier ions are restricted by detection of gamma-rays emitted in their interactions with dense material (see, *e.g.*, Vilmer, MacKinnon, and Hurford, 2011), electrons can be used as their probable tracers. Electrons show up in electromagnetic emission from gamma-ray bremsstrahlung continuum up to long radio waves. In the course of an eruptive flare, electrons and heavier particles are presumably injected from the reconnection site both down, into the flare loops, and up, into the forming flux rope. Then, electrons confined in an expanding flux rope, where heavier particles can also be trapped, are able to produce a drifting Type IV burst. If reconnection between the flux rope and an open magnetic structure grants the trapped particles access to the interplanetary space, then a DH Type III produced by escaping electrons hints at a possible release of heavier particles.

Section 4.3 considered a possible release of electrons trapped in the first flux rope after reconnection of its flank with a streamer or coronal hole, resulting in the Type III-1 burst. Its onset corresponds to a height of the flux-rope's top of $1.55R_{\odot}$ and a possible height of the reconnection site of $0.78R_{\odot}$. Masson, Antiochos, and DeVore (2013) showed a possibility of such SEP release in reconnection between a flux rope and coronal hole. In our event, the distance between AR 9742 and a large southern coronal hole in Figure 4 projected to this height was about $1R_{\odot}$. Due to the extra-radial divergence of magnetic field lines in a coronal hole, its contact with the flux rope at this height appears to be possible, as well as reconnection between the left-handed flux rope with an axial field pointed north-east and the southeasterly S-polarity coronal hole.

The appearance of the magnetic path to the interplanetary space should also release conglomerate of heavier particles trapped in the first flux rope before Type III-1. Appropriate species supplied a rich seed population for acceleration by a trailing shock wave, which arrived in about five minutes, as Figure 16a shows. This probably occurred at one of the flanks of the flux rope and shock wave rather than at their noses.

The estimated height of the second flux-rope's top at the onset of Type III-2 is $2.1 \mathrm{R}_\odot$. The height of the presumable reconnection site is $\approx 1.05 \mathrm{R}_\odot$. Reconnection between the second flux rope expanding extra-radially and the coronal hole at this larger height is still more probable than for the first flux rope. The starting frequency of Type III-2 expected at this height is $6.6 \, \mathrm{MHz}$ (or $21 \, \mathrm{MHz}$ for reconnection with a streamer); actually it was absent at $> 25 \, \mathrm{MHz}$ and certainly present at $< 9 \, \mathrm{MHz}$, as seen from Figure 10 (Section 4.3). Its onset time, 05:27, is close to the SPR time of $05{:}29{:}00 \pm 3.7 \, \mathrm{min}$ estimated by Reames (2009a,b). Note, however, that the heliocentric distances of the particle release during Type III-1 and Type III-2 that we estimate for a CME flank are roughly about $2 \mathrm{R}_\odot$ *vs.* $(3.6 \pm 0.5) \mathrm{R}_\odot$ estimated by Reames (2009a,b) for the CME nose.

The absence of Type III bursts in the metric range during DH Type III-1 and Type III-2 under the presence of accelerated electrons evidenced by flare emissions (Figure 10) indicates the closeness of the magnetic configuration at that time. In contrast, the appearance of a dense metric Type III group associated with DH Type III-3 indicates that the magnetic configuration became open. Particles accelerated in the flare region gained direct access to the interplanetary space. Thus, Type III-3 is a presumable sign that the post-impulsive particle acceleration argued in several studies started (*e.g.* Chertok, 1995; Klein *et al.*, 1999, 2014). Although the related particle flux seems to be weaker than that in the main flare, its contribution can be appreciable at moderate energies due to long durations of post-eruption processes.

6.3.2. Particle Release in Other GLE Events

The preceding section confirms that DH Type III bursts $(1 - 14 \, \mathrm{MHz})$ can trace release of heavy particles. To test how common this pattern is, we glance at the GLEs analyzed by Reames (2009a), for which *Wind*/WAVES data are available. These are 13 out of 16 GLEs of Solar Cycle 23, excluding GLE55, GLE62, and GLE68, whose analysis was problematic. From one to four strong DH Type III bursts were observed in each event. The SPR time estimated by Reames (2009b) from the VDA analysis is typically close to one of these DH Type IIIs and never precedes their group. Coincidence is present in seven events, the interval between a Type III burst and the estimated SPR error band is within five minutes in four events, and the SPR time is considerably later than the Type IIIs in GLE58 (24 August 1998, $\sim 30 \, \mathrm{min}$) and GLE66 (29 October 2003, $\sim 15 \, \mathrm{min}$).

Following traditional hypotheses, Reames (2009a,b) assumes that the shock wave starts to form when the CME exceeds the Alfvén speed ahead it. The onset of a Type II burst is regarded as the onset of the shock formation. The shock is assumed to strengthen afterwards. The SPR time is considered as a sign when the particle acceleration becomes efficient. However, the scenario outlined in the preceding section indicates that the shock wave appears during the flare rise and can accelerate particles much earlier than traditionally assumed.

Reames (2009b) found for the 29 October 2003 event (GLE66) an SPR time of $20{:}55.6 \, \mathrm{ST} \pm 5.8 \, \mathrm{min}$, *i.e.*, $21{:}03{:}56 \, \mathrm{UTC} \pm 5.8 \, \mathrm{min}$ for an observer on Earth. According to Balasubramaniam, Pevtsov, and Neidig (2007), a Moreton wave in

this event started as early as 20:43 UTC and propagated with a speed of $1100-1200\,\mathrm{km\,s^{-1}}$, which certifies its shock-wave regime. A Type II burst was observed in Culgoora (consistent with the Palehua spectrogram) starting at 20:42 UTC from 430 MHz. On the other hand, GLE66 started at 21:05 UTC (Gopalswamy *et al.*, 2012), and the onset of the $> 100\,\mathrm{MeV}$ proton enhancement is detectable in the GOES-10 data at the same time. With a magnetic path length of $1.75 \pm 0.09\,\mathrm{AU}$ (Reames, 2009b), the estimated SPR time appears to be too late.

A key is possibly related to the GLE66 occurrence during the strongest Forbush decrease after 1970s. It was caused by a huge magnetic cloud moving with a very high speed of $1900\,\mathrm{km\,s^{-1}}$ (Grechnev *et al.*, 2014a). Because of its rapid motion, the magnetic path lengths for different-energy particles could not be identical, distorting the results of VDA.

Another exception is GLE58 on 24 August 1998. Reames (2009b) found the SPR time for this event at 22:32.1 ST $\pm 4.6\,\mathrm{min}$, *i.e.* 22:40:26 UTC $\pm 4.6\,\mathrm{min}$. According to Vršnak *et al.* (2002), a Moreton wave started at 22:03 UTC with an initial speed of $946\,\mathrm{km\,s^{-1}}$, decelerated like a blast wave, and was observed up to 500 Mm. A Type II burst started at 22:02 UTC. The shock wave was clearly present early in the event. GLE58 started at 22:50 UTC (Gopalswamy *et al.*, 2012), while the $> 100\,\mathrm{MeV}$ proton enhancement is also detectable at that time. With an estimated path length of $1.55 \pm 0.04\,\mathrm{AU}$, the $100\,\mathrm{MeV}$ protons should leave the Sun before 22:29 UTC. The situation is also challenging.

There was no conspicuous anomaly in the Earth's environment during the GLE58 occurrence. A key can also be related to energy-dependent transport effects (drifts, diffusion, and others), whose importance is prompted by a moderately eastern position of the solar source region (E09 N35). Impressive transport issues were demonstrated by the 1 September 2014 solar event behind the east limb. The rise phase of a related proton enhancement was dominated during half a day by $> 100\,\mathrm{MeV}$ protons, whereas their expected flux should be suppressed.

Most likely, the uncertainties of the VDA results obtained by Reames (2009b) for 13 GLEs of Solar Cycle 23 were underestimated because of not considered transport effects (some corrections in the VDA were analyzed by Laitinen *et al.*, 2015). Presumable realistic SPR times in these GLEs are close to the DH Type III bursts, pointing at concurrent release of heavy particles and electrons, probably accelerated by flare processes. However, the VDA has not revealed an expected earlier population accelerated by shock waves, which should appear during the flare impulsive phase. The shock-accelerated population is certainly expected and can dominate, at least, at low energies. A possible explanation can be that the seed population is supplied by a preceding eruption, like our event. In this case, the ions released from the flux rope should inherit the properties typical of a flare region such as a high iron ionization state (*cf.* Desai *et al.*, 2006). However, this is not always the case (see Section 2). Possibly, material of quiet coronal structures swept up by the top of an expanding flux rope can be somehow implicated. These circumstances call for rethinking the conditions of particle acceleration by shock waves and the signatures of these particles.

Note that magnetic confinement of protons and heavier ions is not as tight as that of electrons. Having much larger gyroradii, heavy particles can escape easier

than electrons. Therefore, DH Type III bursts hint at most effective release of heavy particles, while their escape is possible at different time.

A flux-rope-mediated escape of accelerated protons and electrons is different. The mean free path $[\lambda_i]$ of a fast ion with a mass $[m_i]$, charge $[e_i]$, and an initial velocity $[v_0]$, in plasma with a number density $[n]$ is $\lambda_i = m_i m_e v_0^4 / \left(16\pi e_i^2 e_e^2 \Lambda n\right)$, where $\Lambda \approx 10$ is Coulomb logarithm, $[e_e]$ and $[m_e]$ are the electron charge and mass; $\tau_{\text{coll}} \approx \lambda_i/v_0$. The lifetime of relativistic electrons with an energy $[E_e]$ is $\tau_{\text{life (e)}} \approx 2.6 \times 10^9 E_e/n$. For example, the lifetime of $100\,\text{MeV}$ protons exceeds the lifetime of $0.5\,\text{MeV}$ electrons in the same plasma by two orders of magnitude. Thus, the electron-to-proton ratio escaping from a flux rope with an initial $n > 10^{10}\,\text{cm}^{-3}$ may be much less than for their direct escape from the flare site.

7. Summary

Combining observations available for the 26 December 2001 event in various spectral ranges, it has become possible to reconstruct its scenario and follow the histories of the CME and shock wave. This solar event consisted of the following episodes. i) The first flux-rope's eruption started around 04:30. ii) The second, largest eruption around 05:04 produced the first shock wave and the main CME. iii) The third, jet-like eruption around 05:09 produced the second shock wave. Each wave was most likely excited in the impulsive-piston scenario by a sharply expanding erupting flux rope, rapidly steepened into a shock because of a steep falloff of the fast-mode speed outward from the eruption region, and initially resembled a blast wave. Both waves ultimately merged around the radial direction into a single stronger shock wave. Being followed by a fast CME body, it should eventually change to the bow-shock regime.

1. • The shock wave within the LASCO field of view was in an intermediate regime between the two extremities of blast wave and bow shock. The wave kinematics was controlled by the trailing piston (CME), whose mass grew at the first stage due to the swept-up plasma. This factor missed in many studies determined strong deceleration of the wave at this stage, different from the bow-shock regime, which becomes possible at distances $> 15\text{R}_\odot$.
   • The Type II emission in this event was traced from meters up to $\approx 250\,\text{kHz}$. Two shock waves coexisted at moderate distances from the Sun, which rules out the bow-shock regime at this stage and indicates location of, at least, one of the radio sources at a flank of the shock. Correspondence of a calculated trajectory to the overall observed evolution of the Type II emission in the whole frequency range demonstrates its common origin without any disjoint between the metric and interplanetary Type II emissions.
   • The shock excitation scenario described here was the only in eruptive flares we studied so far with a GOES importance from B to X class. Neither we observed a different overall history of the shock wave ahead of a fast CME.
2. • Shock waves actually appear during the flare rise, being able to accelerate particles much earlier than usually assumed. A delayed particle release time suggests instead their acceleration throughout the flare and accumulation in the flux-rope's magnetic trap until the access to magnetic fields open into

the interplanetary space appears. The latter is possible in reconnection of the flux rope with an open structure. The rate of the particle escape from the trap determining their flux can considerably exceed the rate of their preceding injection into the trap during the flare. This transport scenario can account for the contrast between the strong proton flux and the flare microwave burst, which was not extreme on 26 December 2001.

- The flux-rope-mediated transport scenario is supported by the closeness of the estimated particle release to the DH Type III bursts in most GLE events of Solar Cycle 23. This scenario can also supply a seed population to be accelerated by a trailing shock wave. In this case, particles are most likely released at a flank of an expanding flux rope and shock wave. This results in considerably lesser heights of particle release than usually assumed.

3. The first eruption stretched closed structures above the active region, facilitating escape of flare-accelerated particles and lift-off of the main CME. Having not spent a part of its energy to overcome the magnetic tension of closed structures and sweep up plasma ahead, the main CME was able to reach a higher speed and drive a stronger shock. Thus, the preceding eruption could have amplified the outcome of both flare-accelerated and shock-accelerated protons. Another factor was excitation of two shock waves, eventually merging in a stronger shock. Both these factors can amplify solar particle events.

References

Afanasyev, A.N., Uralov, A.M., Grechnev, V.V.: 2013, *Astron. Rep.*, **57**, 594. DOI

Akinian, S.T., Alibegov, M.M., Kozlovski, V.D., Chertok, I.M: 1978, *Geomagn. Aeron.*, **18**, 410.

Aschwanden, M.J.: 2012, *Space Sci. Rev.* **173**, 3. DOI

Balasubramaniam, K.S., Pevtsov, A.A., Neidig, D.F.: 2007, *Astrophys. J.* **658**, 1372. DOI

Belov, A.V., Eroshenko, E.A., Kryakunova, O.N., Kurt, V.G., Yanke, V.G.: 2010, *Geomagnetism and Aeronomy* **50**, 21. DOI

Bougeret, J.-L., Kaiser, M.L., Kellogg, P.J., Manning, R., Goetz, K., Monson, S.J., Monge, N., Friel, L., Meetre, C.A., Perche, C., Sitruk, L., Hoang, S.: 1995, *Space Sci. Rev.* **71**, 231. DOI

Brueckner, G.E., Howard, R.A., Koomen, M.J., Korendyke, C.M., Michels, D.J., Moses, J.D., Socker, D.G., Dere, K.P., Lamy, P.L., Llebaria, A., *et al.*: 1995, *Solar Phys.* **162**, 357. DOI

Cane, H.V., Erickson, W.C.: 2005, *Astrophys. J.* **623**, 1180. DOI

Castelli, J.P., Barron, W.R.: 1977, *J. Geophys. Res.* **82**, 1275. DOI

Chertok, I.M.: 1995, *International Cosmic Ray Conference* **4**, 78.

Chupp, E.L., Ryan, J.M.: 2009, *Res. Astron. Astrophys.* **9**, 11. DOI

Ciaravella, A., Raymond, J.C., Kahler, S.W.: 2006, *Astrophys. J.* **652**, 774. DOI

Cliver, E.W.: 2006, *Astrophys. J.* **639**, 1206. DOI

Croom, D.L.: 1971, *Solar Phys.* **19**, 171. DOI

Delaboudinière, J.-P., Artzner, G.E., Brunaud, J., Gabriel, A.H., Hochedez, J.F., Millier, F., Song, X.Y., Au, B., Dere, K.P., Howard, R.A., *et al.*: 1995, *Solar Phys.* **162**, 291. DOI

Desai, M.I., Mason, G.M., Gold, R.E., Krimigis, S.M., Cohen, C.M.S., Mewaldt, R.A., Mazur, J.E., Dwyer, J.R.: 2006, *Astrophys. J.* **649**, 470. DOI

Dierckxsens, M., Tziotziou, K., Dalla, S., Patsou, I., Marsh, M.S., Crosby, N.B., Malandraki, O., Tsiropoula, G.: 2015, *Solar Phys.* **290**, 841. DOI

Filippov, B., Golub, L., Koutchmy, S.: 2009, *Solar Phys.* **254**, 259. DOI

Geier, S., Barbier, L.M., Binns, W.R., Christian, E.R., Cummings, J.R., de Nolfo, S.M., Israel, M.H., Link, J.T., Mewaldt, R.A., Mitchell, J.W., *et al.*: 2003, *International Cosmic Ray Conference* **6**, 3261.

Gopalswamy, N., Mäkelä, P., Akiyama, S., Yashiro, S., Xie, H., Thakur, N., Kahler, S.W.: 2015, *Astrophys. J.* **806**, 8. DOI

Gopalswamy, N., Xie, H., Yashiro, S., Akiyama, S., Mäkelä, P., Usoskin, I.G.: 2012, *Space Sci. Rev.* **171**, 23. DOI

Grechnev, V.V.: 2003, *Solar Phys.* **213**, 103. DOI

Grechnev, V.V., Kochanov, A.A.: 2016, *Solar Phys.* **291**, (Article I). DOI

Grechnev, V.V., Lesovoi, S.V., Smolkov, G.Y., Krissinel, B.B., Zandanov, V.G., Altyntsev, A.T., Kardapolova, N.N., Sergeev, R.Y., Uralov, A.M., Maksimov, V.P., Lubyshev, B.I.: 2003, *Solar Phys.* **216**, 239. DOI

Grechnev, V.V., Uralov, A.M., Zandanov, V.G., Rudenko, G.V., Borovik, V.N., Grigorieva, I.Y., Slemzin, V.A., Bogachev, S.A., Kuzin, S.V., Zhitnik, I., Pertsov, A.A., Shibasaki, K., Livshits, M.A.: 2006, *Publ. Astron. Soc. Japan* **58**, 55. DOI

Grechnev, V.V., Kurt, V.G., Chertok, I.M., Uralov, A.M., Nakajima, H., Altyntsev, A.T., Belov, A.V., Yushkov, B.Y., Kuznetsov, S.N., Kashapova, L.K., Meshalkina, N.S., Prestage, N.P.: 2008a, *Solar Phys.* **252**, 149. DOI

Grechnev, V.V., Uralov, A.M., Slemzin, V.A., Chertok, I.M., Kuzmenko, I.V., Shibasaki, K.: 2008b, *Solar Phys.* **253**, 263. DOI

Grechnev, V.V., Uralov, A.M., Chertok, I.M., Kuzmenko, I.V., Afanasyev, A.N., Meshalkina, N.S., Kalashnikov, S.S., Kubo, Y.: 2011, *Solar Phys.* **273**, 433. DOI

Grechnev, V.V., Kiselev, V.I., Uralov, A.M., Meshalkina, N.S., Kochanov, A.A.: 2013a, *Publ. Astron. Soc. Japan* **65**, SP1, S9. DOI

Grechnev, V.V., Meshalkina, N.S., Chertok, I.M., Kiselev, V.I.: 2013b, *Publ. Astron. Soc. Japan* **65**, SP1, S4. DOI

Grechnev, V.V., Uralov, A.M., Chertok, I.M., Belov, A.V., Filippov, B.P., Slemzin, V.A., Jackson, B.V.: 2014a, *Solar Phys.* **289**, 4653. DOI

Grechnev, V.V., Uralov, A.M., Chertok, I.M., Slemzin, V.A., Filippov, B.P., Egorov, Ya.I., Fainshtein, V.G., Afanasyev, A.N., Prestage, N., Temmer, M.: 2014b, *Solar Phys.* **289**, 1279. DOI

Grechnev, V.V., Kiselev, V.I., Meshalkina, N.S., Chertok, I.M.: 2015a, *Solar Phys.* **290**, 2827. DOI

Grechnev, V.V., Uralov, A.M., Kuzmenko, I.V., Kochanov, A.A., Chertok, I.M., Kalashnikov, S.S.: 2015b, *Solar Phys.* **290**, 129. DOI

Grechnev, V.V., Uralov, A.M., Kochanov, A.A., Kuzmenko, I.V., Prosovetsky, D.V., Egorov, Y.I., Fainshtein, V.G., Kashapova, L.K.: 2016, *Solar Phys.* **291**, 1173. DOI

Grechnev, V.V., Uralov, A.M., Kiselev, V.I., Kochanov, A.A.: 2017, *Solar Phys.* **292: 3.** (Article II). DOI

Handy, B.N., Acton, L.W., Kankelborg, C.C., Wolfson, C.J., Akin, D.J., Bruner, M.E., Caravalho, R., Catura, R.C., Chevalier, R., Duncan, D.W., *et al.*: 1999, *Solar Phys.* **187**, 229. DOI

Kahler, S.W.: 1982, *J. Geophys. Res.* **87**, 3439. DOI

Kallenrode, M.-B.: 2003, *J. Phys. G Nuclear Phys.* **29**, 965. DOI

Klein, K.-L., Trottet, G.: 2001, *Space Sci. Rev.* **95**, 215. DOI

Klein, K.-L., Mouradian, Z.: 2002, *Astron. Astrophys.* **381**, 683. DOI

Klein, K.-L., Chupp, E.L., Trottet, G., Magun, A., Dunphy, P.P., Rieger, E., Urpo, S.: 1999, *Astron. Astrophys.* **348**, 271.

Klein, K.-L., Masson, S., Bouratzis, C., Grechnev, V., Hillaris, A., Preka-Papadema, P.: 2014, *Astron. Astrophys.* **572**, AA4. DOI

Knock, S.A., Cairns, I.H.: 2005, *J. Geophys. Res.* A **110**, A01101. DOI

Kwon, R.-Y., Zhang, J., Olmedo, O.: 2014, *Astrophys. J.* **794**, 148. DOI

Kwon, R.-Y., Zhang, J., Vourlidas, A.: 2015, *Astrophys. J. Lett.* **799**, L29. DOI

Laitinen, T., Huttunen-Heikinmaa, K., Valtonen, E., Dalla, S.: 2015, *Astrophys. J.* **806**, 114. DOI

Lario, D., Aran, A., Decker, R.B.: 2009, *Solar Phys.* **260**, 407. DOI

Mann, G., Klassen, A., Aurass, H., Classen, H.-T.: 2003, *Astron. Astrophys.* **400**, 329. DOI

Masson, S., Antiochos, S.K., and DeVore, C.R.: 2013, *Astrophys. J.* **771**, 82. DOI

Masson, S., Pariat, E., Aulanier, G., Schrijver, C.J.: 2009, *Astrophys. J.* **700**, 559. DOI

McLean, D.J.: 1973, *Proc. Astron. Soc. Australia* **2**, 222.

Melnikov, V.F., Podstrigach, T.S., Dajbog, E.I., Stolpovskij, V.G.: 1991, *Cosmic Research* **29**, 87.

Meshalkina, N.S., Uralov, A.M., Grechnev, V.V., Altyntsev, A.T., Kashapova, L.K.: 2009, *Publ. Astron. Soc. Japan* **61**, 791. DOI

Mewaldt, R.A., Looper, M.D., Cohen, C.M.S., Haggerty, D.K., Labrador, A.W., Leske, R.A., Mason, G.M., Mazur, J.E., von Rosenvinge, T.T.: 2012, *Space Sci. Rev.* **171**, 97. DOI

Miklenic, C.H., Veronig, A.M., Vršnak, B.: 2009, *Astron. Astrophys.* **499**, 893. DOI

Miroshnichenko, L.I., Vashenyuk, E.V., Pérez-Peraza, J.A.: 2013, *Geomag. Aeron.* **53**, 541. DOI

Nakajima, H., Nishio, M., Enome, S., Shibasaki, K., Takano, T., Hanaoka, Y., Torii, C., Sekiguchi, H. *et al.*: 1994, *Proc. IEEE* **82**, 705. DOI

Nakajima, H., Sekiguchi, H., Sawa, M., Kai, K., Kawashima, S.: 1985, *Publ. Astron. Soc. Japan* **37**, 163.

Neupert W.M.: 1968, *Astrophys. J. Lett.* **153**, L59. DOI

Newkirk, G. Jr.: 1961, *Astrophys. J.* **133**, 983. DOI

Nitta, N.V., Liu, Y., DeRosa, M.L., Nightingale, R.W.: 2012, *Space Sci. Rev.* **171**, 61. DOI

Qiu J., Hu Q., Howard T., Yurchyshyn V.: 2007, *Astrophys. J.* **659**, 758. DOI

Reames, D.V.: 2009a, *Astrophys. J.* **693**, 812. DOI

Reames, D.V.: 2009b, *Astrophys. J.* **706**, 844. DOI

Reames, D.V.: 2013, *Space Sci. Rev.* **175**, 53. DOI

Reiner, M.J., Vourlidas, A., St. Cyr, O.C., Burkepile, J.T., Howard, R.A., Kaiser, M.L., Prestage, N.P., Bougeret, J.-L.: 2003, *Astrophys. J.* **590**, 533. DOI

Rouillard, A.P., Sheeley, N.R., Tylka, A., Vourlidas, A., Ng, C.K., Rakowski, C., Cohen, C.M.S., Mewaldt, R.A., Mason, G.M., Reames, D., Savani, N.P., StCyr, O.C., Szabo, A.: 2012, *Astrophys. J.* **752**, 44. DOI

Saito, K.: 1970, *Ann. Tokyo Astr. Obs.* **12**, 53.

Saito, K., Poland, A.I., and Munro, R.H.: 1977, *Solar Phys.* **55**, 121. DOI

Sheeley, N.R., Wang, Y.-M., Hawley, S.H., Brueckner, G.E., Dere, K.P., Howard, R.A., Koomen, M.J., Korendyke, C.M., Michels, D.J., Paswaters, S.E., *et al.*: 1997, *Astrophys. J.* **484**, 472.

Smolkov, G.I., Pistolkors, A.A., Treskov, T.A., Krissinel, B.B., Putilov, V.A.: 1986, *Astrophys. Spa. Sci.* **119**, 1. DOI

Temmer, M., Veronig, A.M., Vršnak, B., Rybák, J., Gömöry, P., Stoiser, S., Maričić, D.: 2008, *Astrophys. J.* **673**, 95. DOI

Temmer, M., Veronig, A., Kontar, E., Krucker, S., Vršnak, B.: 2010, *Astrophys. J.* **712**, 1410. DOI

Trottet, G., Samwel, S., Klein, K.-L., Dudok de Wit, T., Miteva, R.: 2015, *Solar Phys.* **290**, 819. DOI

Tylka, A.J., Cohen, C.M.S., Dietrich, W.F., Lee, M.A., Maclennan, C.G., Mewaldt, R.A., Ng, C.K., Reames, D.V.: 2005, *Astrophys. J.* **625**, 474. DOI

Tylka, A.J., Malandraki, O.E., Dorrian, G., Ko, Y.-K., Marsden, R.G., Ng, C.K., Tranquille, C.: 2013, *Solar Phys.* **285**, 251. DOI

Uralov, A.M., Grechnev, V.V., Rudenko, G.V., Myshyakov, I.I., Chertok, I.M., Filippov, B.P., Slemzin, V.A.: 2014, *Solar Phys.* **289**, 3747. DOI

Uralova, S.V., Uralov, A.M.: 1994, *Solar Phys.* **152**, 457. DOI

Vilmer, N., MacKinnon, A.L., Hurford, G.J.: 2011, *Space Sci. Rev.* **159**, 167. DOI

Vršnak, B., Cliver, E.W.: 2008, *Solar Phys.* **253**, 215. DOI

Vršnak, B., Warmuth, A., Brajša, R., Hanslmeier, A.: 2002, *Astron. Astrophys.* **394**, 299. DOI

Yashiro, S., Gopalswamy, N., Michalek, G., St. Cyr, O.C., Plunkett, S.P., Rich, N.B., Howard, R.A.: 2004, *J. Geophys. Res.* **109**, A07105. DOI

Zhang, J., Dere, K.P., Howard, R.A., Kundu, M.R., White, S.M.: 2001, *Astrophys. J.* **559**, 452. DOI